


การประเมินโครงสร้างระดับไมโครของฟิล์มควมิกอินเดียมไนไตรด์ที่ปลูกผลึกโดย
โมเลกุลาร์บีมเอพีแทกซี



นางสาวปภากร จันทะวงศ์ฤทธิ

วิทยานิพนธ์นี้เป็นส่วนหนึ่งของการศึกษาตามหลักสูตรปริญญาวิทยาศาสตรมหาบัณฑิต
สาขาวิชาฟิสิกส์ ภาควิชาฟิสิกส์
คณะวิทยาศาสตร์ จุฬาลงกรณ์มหาวิทยาลัย
ปีการศึกษา 2551
ลิขสิทธิ์ของจุฬาลงกรณ์มหาวิทยาลัย

MICROSTRUCTURAL ASSESSMENT OF CUBIC InN FILM GROWN BY
MOLECULAR BEAM EPITAXY



Miss Papaporn Jantawongrit

A Thesis Submitted in Partial Fulfillment of the Requirements
for the Degree of Master of Science Program in Physics

Department of Physics

Faculty of Science


Chulalongkorn University

Academic year 2008

Copyright of Chulalongkorn University


Thesis Title MICROSTRUCTURAL ASSESSMENT OF CUBIC InN
FILM GROWN BY MOLECULAR BEAM EPITAXY
By Miss Papaporn Jantawongrit
Field of Study Physics
Advisor Assistant Professor Sakuntam Sanorpim, Ph.D.
Co-Advisor Chanchana Thanachayanont, Ph.D.


Accepted by the Faculty of Science, Chulalongkorn University in Partial
Fulfillment of the Requirements for the Master's Degree

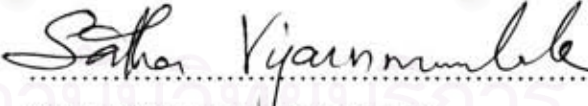

..... Dean of the Faculty of Science
(Professor Supot Hannongbua, Ph.D.)


THESIS COMMITTEE


..... Chairman
(Assistant Professor Pornchai Pacharintanakun, Ph.D.)


..... Advisor
(Assistant Professor Sakuntam Sanorpim, Ph.D.)


..... Co-Advisor
(Chanchana Thanachayanont, Ph.D.)


..... Examiner
(Sathon Vijarnwanmaluk, Ph.D.)


..... External Examiner
(Assistant Professor Patcharee Pratumpong, Ph.D.)

ปกสาร จันทะวงศ์ฤทธิ์: การประเมินโครงสร้างระดับไมโครของฟิล์มคิวบิกอินเดียมไนไตรด์ที่ปลูกผลึกโดยโมเลกุลาร์บีมเอพิแทกซี. (MICROSTRUCTURAL ASSESSMENT OF CUBIC InN FILM GROWN BY MOLECULAR BEAM EPITAXY) อ.ที่ปรึกษา
 วิทยานิพนธ์หลัก: ผศ.ดร.สกุลธรรม เสนาะพิมพ์ อ.ที่ปรึกษาวิทยานิพนธ์ร่วม: ดร.ชญชญา
 ธนชยานนท์, 59 หน้า.

ในวิทยานิพนธ์ การเปลี่ยนแปลงโครงสร้างและคุณภาพผลึกของฟิล์มคิวบิกอินเดียมไนไตรด์ (cubic InN หรือ *c*-InN) ที่ปลูกผลึกลงบนแกเลียมอาร์เซไนด์ (GaAs) ชั้นสเตรตที่มีผิวระนาบ (001) โดยวิธีโมเลกุลาร์บีมเอพิแทกซีได้ถูกตรวจสอบและวิเคราะห์อย่างเป็นระบบ อิทธิพลจากเงื่อนไขการปลูก คือ สภาพการปลูกที่มีอินเดียมและไนโตรเจนที่มากเกินไป จากการวัดการเลี้ยวเบนกำลังแยกสูง พบว่าฟิล์มบาง InN ที่ถูกใช้ในการศึกษานี้มีโครงสร้างหลักแบบคิวบิก นอกจากนี้ภาพไมโครกราฟชนิดภาคตัดขวางและผลจากการเลี้ยวเบนของอิเล็กตรอนที่วัดจากกล้องจุลทรรศน์อิเล็กตรอนชนิดส่องผ่าน แสดงให้เห็นว่า ฟิล์มบาง *c*-InN ที่ปลูกภายใต้สภาวะที่มีอินเดียมที่มากเกินไป มีแถบความบกพร่องชนิดสแตกกิ้งฟอลท์ ซึ่งวางตัวอยู่บนระนาบ (111) โดยที่ความหนาแน่นของสแตกกิ้งฟอลท์ลดลงตามความหนาของฟิล์มจะมีความหนาแน่นน้อยที่บริเวณห่างจากผิวรอยต่อระหว่าง *c*-InN และ GaAs จากการวิเคราะห์โครงสร้างผลึกไม่พบการก่อเกิดของโครงสร้างผลึกแบบเฮกซะโกนัลในฟิล์มบางที่ถูกปลูกภายใต้สภาวะที่มีอินเดียมที่มากเกินไป นอกจากนี้ ผลจากการเลี้ยวเบนของอิเล็กตรอนได้แสดงให้เห็นว่า ฟิล์มบาง *c*-InN ที่ปลูกภายใต้สภาวะที่มีไนโตรเจนมากเกินไป แสดงการเปลี่ยนโครงสร้างเดี่ยวแบบคิวบิกไปเป็นโครงสร้างผสมระหว่างโครงสร้างแบบคิวบิกและแบบเฮกซะโกนัล นอกจากนี้ผลที่ได้จากการกระเจิงแบบรามานสามารถยืนยันได้ว่าโครงสร้างเดี่ยวแบบคิวบิกเปลี่ยนไปเป็นโครงสร้างผสมระหว่างโครงสร้างแบบคิวบิกและโครงสร้างแบบเฮกซะโกนัล ภายใต้สภาวะไนโตรเจนที่มากเกินไป ในงานวิจัยนี้ได้แสดงให้เห็นเงื่อนไขการปลูกที่เป็นปัจจัยสำคัญในการปลูกผลึกฟิล์มบาง *c*-InN ให้มีความบริสุทธิ์สูงลดความบกพร่องเชิงระนาบและลดการก่อเกิดของโครงสร้างเดี่ยวแบบ *h*-InN ในฟิล์มบาง *c*-InN

ภาควิชา.....ฟิสิกส์.....
 สาขาวิชา.....ฟิสิกส์.....
 ปีการศึกษา.....2551.....

ลายมือชื่อนิสิต.....ปกสาร จันทะวงศ์ฤทธิ์.....
 ลายมือชื่อ.ที่ปรึกษาวิทยานิพนธ์หลัก.....
 ลายมือชื่อ.ที่ปรึกษาวิทยานิพนธ์ร่วม.....

4972358523: MAJOR PHYSICS

KEYWORDS: TRANSMISSION ELECTRON MICROSCOPY /STRUCTURAL DEFECTS / MOLECULAR BEAM EPITAXY

PAPAPORN JANTAWONGRIT: MICROSTRUCTURAL ASSESSMENT OF CUBIC InN FILM GROWN BY MOLECULAR BEAM EPITAXY. ADVISOR: ASST. PROF. SAKUNTAM SANORPIM, PH.D., CO-ADVISOR: CHANCHANA THANACHAYANONT, PH.D., 59 pp.

In the thesis, structural modification and crystal quality of cubic InN (*c*-InN) films grown on GaAs (001) substrates by molecular beam epitaxy have been systematically investigated and analyzed. The effects of growth conditions, namely In- and N-rich conditions, are established. Based on high-resolution X-ray diffraction, the result demonstrates that all the InN grown films have a cubic structure. On the other hand, electron diffraction (ED) pattern and cross-sectional transmission electron microscopy (TEM) micrographs demonstrate that the InN grown films contain a high density of stacking faults (SFs) parallel to (111) planes. Besides, the density of SF and twin defects decreases with the distance from the interface of *c*-InN/GaAs. No different type of single diffraction spots on the ED pattern was observed. On the other hand, TEM micrographs the ED patterns demonstrate that the *c*-InN films exhibited a transition from cubic to mixed cubic/hexagonal phase under N-rich growth conditions. In addition, μ -Raman scattering spectra obtained from these InN layers confirmed the existence of a structural modification from cubic to mixed cubic/hexagonal phase in microstructure of the N-rich layers, which exhibit higher hexagonal-phase incorporation than that of the In-rich layers. Our results suggest that the growth condition is a key parameter in the growth of high cubic phase purity *c*-InN films with lower incorporation of single-crystal *h*-InN.

Department:Physics.....

Field of Study: ...Physics.....

Academic Year: .2008.....

Student's Signature.....
 Advisor's Signature.....
 Co-Advisor's Signature.....

Acknowledgements

I would like to express my sincere gratitude to Assistant Professor Dr. Sakuntam Sanorpim and Chanchana Thanachayanont for guidance, valuable suggestions, useful discussions and encouragement throughout my study.

I would like to thank Assistant Professor Dr. Pornchai Pacharintanakun, Dr. Sathon Vijarnwannaluk, and Dr. Patcharee Pratumpong for serving as chairman and committee, respectively. Their comments on this thesis are also greatly appreciated.

I would like to thank the V. Yodsri, National Metal and Materials Technology Center (MTEC), Thailand, for her helpful cooperation in TEM measurements. Sincere thanks are extended to M. Tirarattanasompot, Scientific and Technology Research Equipment Centre (STREC) of Chulalongkorn University, for his technical support in X-ray diffraction measurements. This work has been supported by Thailand Research Fund (contact No MRG5080141), and The 90th Anniversary of Chulalongkorn University Fund (Ratchadaphiseksomphot Endowment Fund).

I would like to acknowledge Department of Physics, Faculty of Science, Chulalongkorn University for providing teaching. Special thank goes to Professor Dr. Kentaro Onabe, Department of Advanced Materials Science, Graduate Schools of Frontier Science, and The University of Tokyo, Japan for providing the great samples.

I would like to thank my friend, Pawinee Klangtakai, Dares Kawket and my senior for useful discussion and joyful moment.

Lastly, I would like to very thank to my family; my father, my mother and my brother for love, understanding, supports and everything.

Contents

	Page
Abstract (Thai)	iv
Abstract (English)	v
Acknowledgements	vi
Contents	vii
List of Tables	ix
List of Figures	x
 Chapter	
I Introduction	1
1.1. Properties and structures of InN.....	1
1.2. Material problems.....	1
1.3. Objectives and organization of the thesis.....	7
II Structural properties and characterization	8
2.1 Epitaxial growth.....	8
2.2 Strained relaxation.....	8
2.3 Generation of defects in epitaxial films.....	9
2.4 Structural characterization.....	11
2.4.1 High resolution X-ray diffraction.....	11
2.4.2 Raman scattering.....	13
2.4.3 Transmission electron microscopy.....	16
III Experiments	27
3.1 MBE growth information of <i>c</i> -InN films.....	27
3.2 TEM specimen preparation.....	28
IV Results and discussion of cubic InN grown on GaAs	33
4.1 Growth information of <i>c</i> -InN	33
4.2 Identification of growth conditions.....	34
4.3 Crystal structure of <i>c</i> -InN.....	35

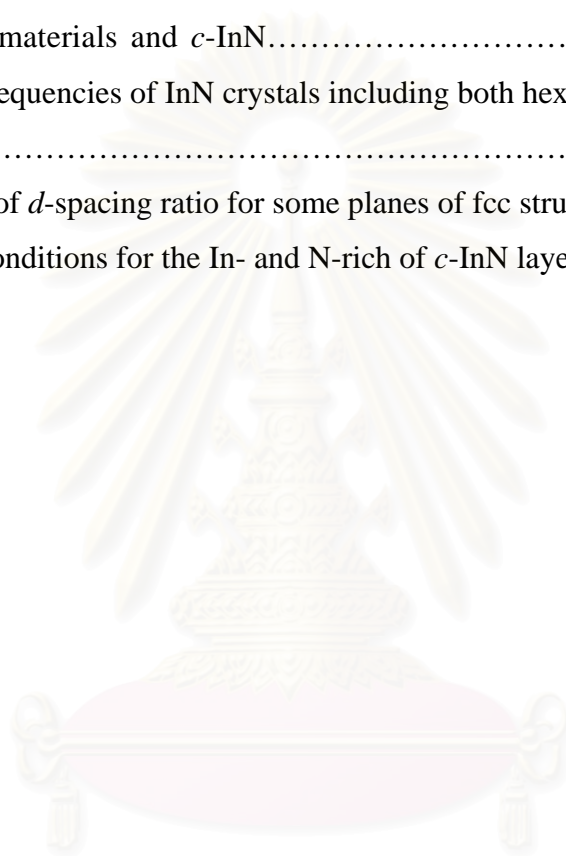
Chapter	Page
4.4	Vibrational properties.....36
4.5	Morphological investigation <i>c</i> -InN.....37
4.6	Microstructure investigation.....39
4.7	Effects of In- and N-rich growth conditions.....41
4.8	Summary.....50
V	Conclusions.....52
	References.....53
	Appendix.....57
	Vitae.....59



สถาบันวิทยบริการ
จุฬาลงกรณ์มหาวิทยาลัย

List of Tables

Table	Page
1.1 Lattice constants, lattice mismatch and thermal expansion coefficients between substrate materials and <i>c</i> -InN.....	4
2.1 Phonon frequencies of InN crystals including both hexagonal and cubic crystal lattices.....	15
2.2 The ratio of <i>d</i> -spacing ratio for some planes of fcc structure	24
4.1 Growth conditions for the In- and N-rich of <i>c</i> -InN layers	34



สถาบันวิทยบริการ
จุฬาลงกรณ์มหาวิทยาลัย

List of Figures

Figure	Page
1.1 Relationship between bandgap energy and lattice constant of some compound semiconductors.....	2
1.2 Schematic illustration of InN crystal structures, (a) hexagonal (wurtzite) structure, (b) cubic (zinc blend), (c) hexagonal structure along $\langle 0001 \rangle$ direction and (d) cubic structure along $\langle 111 \rangle$	3
1.3 Two-dimensional atomic models of crystal structure for InN along (-110) cross-section, (a) cubic structure and (b) hexagonal structure.....	5
1.4 Schematic illustration of possible of planar defects in c-InN film along (-110) cross-section, (a) stacking faults, (b) twins and (c) hexagonal phase subdomain.....	6
2.1 Schematic illustration of (a) lattice-matched layer, (b) fully strained layer and (c) fully relaxed layer heteroepitaxial structures.....	10
2.2 Schematic diagram of Bragg's law.....	12
2.3 Schematic representation of Raman scattering of a photon with (a) emission and (b) absorption of a phonon	15
2.4 Schematic illustration of transmission electron microscopy (TEM).....	17
2.5 Diffraction pattern of diamond silicon showing the relationship between objective apertures and TEM images. The Bright field or Dark field image is formed by selecting the transmit beam (T) or the diffracted beam (D) respectively by using an objective aperture.....	18
2.6 Ewald sphere construction in 2 dimensions. Section through the sphere of reflection containing the incident beam vector (\vec{k}_i), the diffraction beam vector (\vec{k}_d) and reciprocal lattice vector (g_{410})	19
2.7 The face-centered cubic lattice (a) showing a possible reflecting plane (111) and (b) part of its reciprocal lattice.....	21
2.8 Schematic diagram of electron diffraction in TEM.....	22

Figure	Page
2.9	Diffraction pattern of InN along [1-10] zone axis.....23
2.10	Examples of how spots in reciprocal space have different shapes, depending on the shape of the particles which are diffracting.....25
2.11	Streaking of reciprocal lattice points arising from stacking fault parallel to the electron beam.....26
3.1	Schematic illustration of the <i>c</i> - InN film used in this study27
3.2	(a) Cutting instrument low speed diamond wheel saw, (b) Cut specimen on the microscope slide.....29
3.3	(a) Schematic diagram of sticking 2 surface specimens, (b) Clamped specimen, (c) 80 °C for 24 hours heating on the hot plate, (d) Specimen on the triangle glass holder.....29
3.4	(a) Diamond lapping films, (b) Polishing machine29
3.5	Ion beam milling machine30
3.6	Schematic diagram of high-resolution X-ray instrument (Bruker-AXS D8 DISCOVER) at Scientific and Technology Research Equipment Center, Chulalongkorn University.....31
3.7	Schematic drawing of Raman scattering system.....32
4.1	Schematic illustration of <i>c</i> - InN film grown on GaAs (001) substrate.....33
4.2	Scanning electron microscopy (SEM) image of the <i>c</i> -InN grown surfaces at different growth temperatures and supplied N ₂ flow rates. White spots in samples A, B and C indicate the In droplets.....35
4.3	2θ/ω-scan HRXRD (002) profiles of the <i>c</i> -InN films grown on GaAs (001) under In- and N-rich growth condition.....36
4.4	Raman spectra of the <i>c</i> -InN films grown under In-(blue solid curves) and N-(red-solid curves) rich growth conditions. Black-dashed lines and green-dotted lines indicate the characteristic phonon frequencies of <i>c</i> -InN and h-InN phases, respectively.....37

Figure	Page
4.5	Cross-sectional SEM images of the <i>c</i> -InN layers grown on GaAs (001) substrate under the In-rich conditions (at 490°C with the N ₂ flow rate of 1.50 sccm.) and the N-rich conditions (at 450°C with the N ₂ flow rate of 1.75 sccm.), as shown in Figs. 4.5(a) and 4.5(b), respectively.....38
4.6	(a) Cross-sectional TEM image of <i>c</i> -InN film on GaAs (001) substrate grown under the In-rich conditions (at 490°C with the N ₂ flow rate of 1.5 sccm) and (b) Electron diffraction patterns taken from the <i>c</i> -InN/GaAs region along the [1-10] zone ax.....40
4.7	(a) Cross-sectional TEM images for <i>c</i> -InN film on GaAs (001) substrate at different growth condition of (a) under the In-rich conditions (at 490°C with the N ₂ flow rate of 1.5 sccm) and (c) under the N-rich conditions (at 450°C with the N ₂ flow rate of 1.75 sccm). (b) and (d) corresponding electron diffraction patterns taken from the <i>c</i> -InN region along the [1-10] zone axis of Fig.4.7(a) and 4.7(c), respectively.....42
4.8	(a) Electron diffraction patterns records along the [1-10] _{<i>c</i>-InN} zone axis from the InN region containing the pyramid-like structures, (b), (c) and (d) show schematic representation cubic and hexagonal phase related diffraction spots, respective ...43
4.9	Dark field images of <i>c</i> -InN film on GaAs (001) substrate grown under the In-rich conditions (at 490°C with the N ₂ flow rate of 1.5 sccm) which were taken with reflections along (a) $g = (111)$, (b) $g = (002)$ and (c) $g = (220)$ planes. Inset (A), (B) and (C) showing ED patterns were taken form (111), (002) and (220) diffraction shown in (a), (b) and (c), respective. Zone axes is [1-10].....45
4.10	Dark field images of <i>c</i> -InN film on GaAs (001) substrate grown under the N-rich conditions (at 450°C with the N ₂ flow rate of 1.75 sccm) which were taken with reflections along (a) $g = (111)$, (b) $g = (002)$ and (c) $g = 220$ planes. Inset (A), (B) and (C) showing ED patterns were taken form (111), (002) and (220) diffraction shown in (a), (b) and (c), respective. Zone axes is [1-10].....46

Figure	Page
4.11 Dark field images of <i>c</i> -InN film on GaAs (001) substrate grown under the In-rich conditions (at 490°C with the N ₂ flow rate of 1.5 sccm) which were taken with reflections along (a) $g = (111)$, (b) $g = (-1101)$ and (c) $g = (110-1)$ planes. Inset (A), (B) and (C) showing ED patterns were taken from (111), (-1101) and (110-1) diffraction spots shown in (a), (b) and (c), respective. Zone axes is $[1-10]/[11-20]$	48
4.12 Dark field images of <i>c</i> -InN film on GaAs (001) substrate grown under the N-rich conditions (at 450°C with the N ₂ flow rate of 1.75 sccm) which were taken with reflections along (a) $g = (111)$, (b) $g = (-1101)$ and (c) $g = (110-1)$ planes. Inset (A), (B) and (C) showing ED patterns were taken from (111), (-1101) and (110-1) diffraction spots shown in (a), (b) and (c), respective. Zone axes is $[1-10]/[11-20]$	49

CHAPTER I

INTRODUCTION

1.1 InN

III-nitride compound semiconductors, i. e. AlN, GaN and InN, have received intensive interest due to their potential for optoelectronic and electronic devices, such as light emitting diodes (LEDs) [1, 3], light diodes (LDs) [2] and solar cells [3]. Particularly, InN has received attention because its band gap has found to be about 0.6-0.8 eV [1, 4-6], which is much smaller than the previously reported value of about 1.9 eV [7-9]. In Fig.1.1, in addition, its use along with GaN and AlN makes a possibility to extend the light emission of nitride-based LEDs from the ultraviolet to the near infrared wavelength.

Generally, InN has two crystal structures, which are cubic (zincblende) structure and hexagonal (wurtzite) structure. Figure 1.2 shows schematic illustrations of the hexagonal and the cubic structures. It is theoretically predicted that the cubic phase InN (*c*-InN) has advantages over hexagonal-phase InN (*h*-InN), such as high electron mobility, due to weaker phonon scattering and low electron effective mass [10]. These reasons have motivated the study of *c*-InN as a potential material for infrared or high speed electronic device applications. Therefore, the growth of high quality *c*-InN is very important. Recently, *c*-InN films have been successfully grown on GaAs (001) substrate with InAs buffer layer [11], r-plane sapphire [12], 3C-SiC [13] and yttria-stabilized zirconia (YSZ) (001) substrates [14].

1.2 Material problems

Commonly, InN exists as the metastable cubic or the stable hexagonal polytypes. Due to the large different lattice-constants (namely, lattice mismatch) and thermal expansion coefficients (namely, thermal mismatch) between InN and its substrates, stabilization of the *c*-InN crystal is difficult and the growth often results in

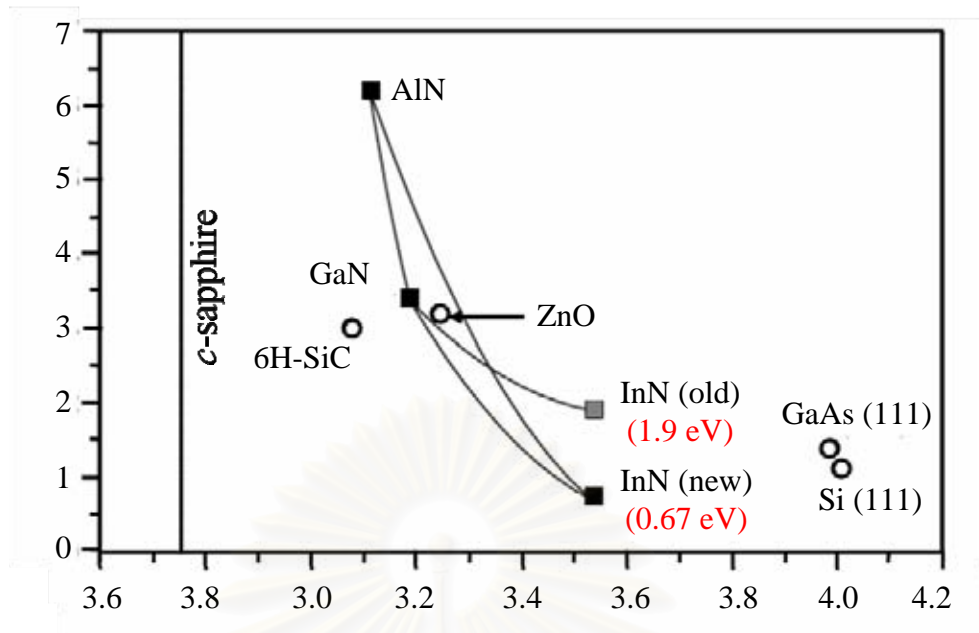


Figure 1.1: Relationship between bandgap energy and lattice constant of III-nitride semiconductors and some interesting compound semiconductors [3]

the mixture phase structures [15]. Using a thin film growth technique such as MBE, it is possible to grow InN and its alloys in the cubic structure. Example is the growth of InN on (001) substrates [15] where the four-fold symmetry of the underlying layer causes adsorption of the metastable cubic structure rather than the lowest energy hexagonal structure. However, high quality *c*-InN films with high cubic-phase purity are still difficult to prepare due to the metastable nature of *c*-InN and the lack of suitable substrate materials [1-5, 15]. These problems lead to generation of structural defects. The first problem is due to the metastable nature of cubic phase, the hexagonal phase is often unexpectedly introduced in cubic layer. Several research groups reported that there are incorporation of hexagonal phase in cubic phase as a formation of planar defect such as twins, stacking faults (SFs) and hexagonal phase subdomain [16, 17]. Such formation of planar defects is common existing on the *c*-InN (111) and *h*-InN (0001) planes. As shown in Fig. 1.2, hexagonal structure can be easily constructed along the $\langle 111 \rangle // \langle 0001 \rangle$ direction. This is because the fundamental difference between these two crystal structures (cubic and hexagonal structures) is merely a 60° rotation along the *h*-InN $\langle 0001 \rangle$ (Figs. 1.2(c)) and 1.3(b)) and *c*-InN $\langle 111 \rangle$ (Figs. 1.2(d) and 1.3(a)) directions [18]. Figure 1.4 shows a schematic diagram of the models describing the generation of planar defects.

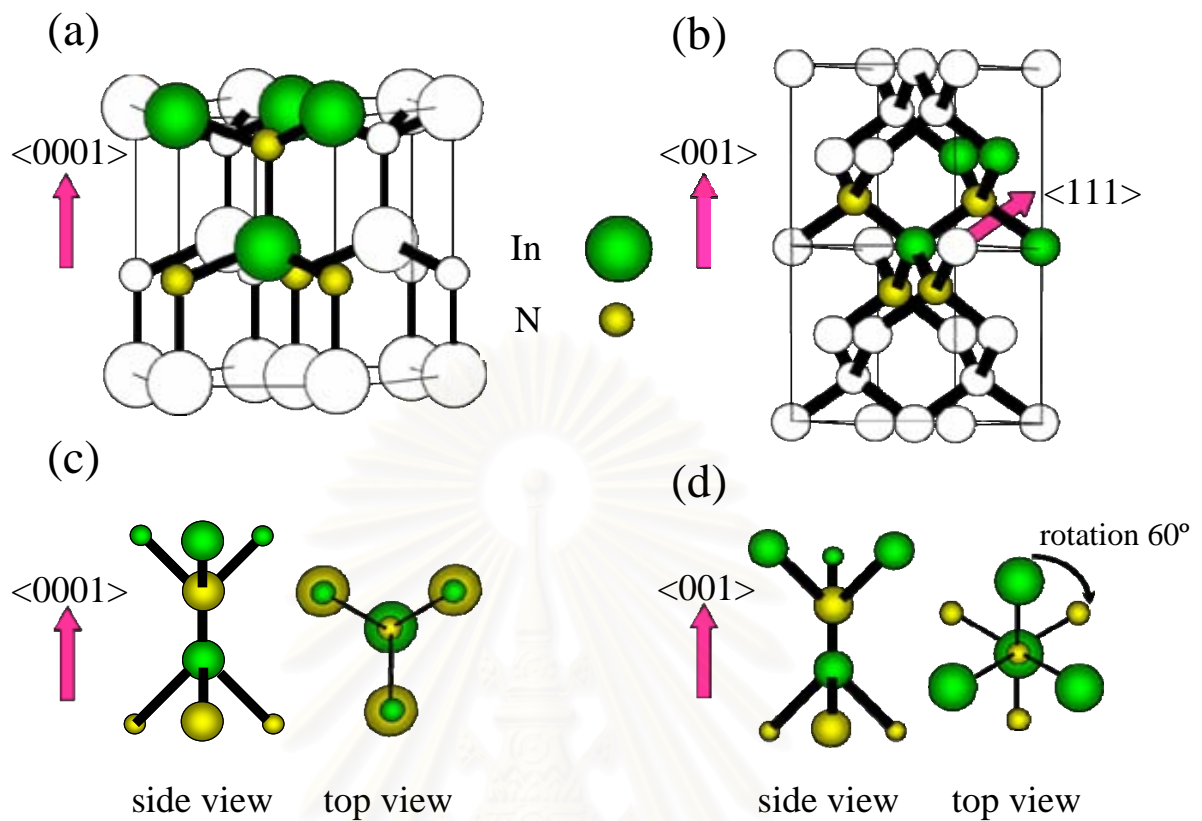


Figure 1.2: Schematic illustration of InN crystal structures, a) hexagonal (wurtzite), (b) cubic (zinc blend), (c) hexagonal structures along $\langle 0001 \rangle$ direction and (d) cubic structure along $\langle 111 \rangle$ direction [32]

There are a number of common properties such as:

- (1) SFs on the cubic $\{111\}$ planes are formed by an insertion of 1 monolayer of hexagonal structure between two cubic structures, which there are identical crystal orientations (Fig. 1.4(a)).
- (2) Twins on the cubic $\{111\}$ planes are formed by an insertion of a half monolayer of hexagonal structure between the two cubic structures, which are different crystal orientations (Fig. 1.4(b)).
- (3) Hexagonal phase subdomain on the cubic $\{111\}$ planes is formed by the extension of SFs to be a single crystal of hexagonal structure (Fig. 1.4(c)).

Substrate materials	Lattice constant (Å)	Lattice mismatch (%)	Thermal expansion coefficients ($\times 10^{-6} \text{ K}^{-1}$)
<i>c</i> -InN	4.98	0	3.8
<i>c</i> -GaN	4.50	10.67	3.17
MgO	4.216	18.29	10.5
GaAs	5.653	-11.90	6
3C-SiC	4.359	14.23	3.9

Table 1.1: Lattice constants, lattice mismatch and thermal expansion coefficients between substrate materials and *c*-InN [3, 19]

Another problem that affects the crystal quality of *c*-InN is a lack of suitable substrate materials. Table 1.1 summarizes the lattice constants and thermal expansion coefficients of *c*-InN and some substrate materials [19]. As shown in the Table a large lattice mismatch and a large difference in thermal expansion coefficients between *c*-InN and those substrate materials lead to a high density of structure defects such as twin, stacking fault and dislocations in InN epitaxy films.

To improve the film quality of *c*-InN, there has been several research groups studied and investigated for the affecting parameters, such growth method, growth condition, substrate material, etc. In fact, the high quality *c*-InN films were achievable grown by MBE on GaAs (001) [20] and MgO (001) [21] substrates despite the large mismatch. However, there are a number of structure defects, which degrade the optical and crystal qualities.

In this work, we focus on growth condition, namely In- and N-rich growth conditions, which may result in the generation of structure defects during the growth.

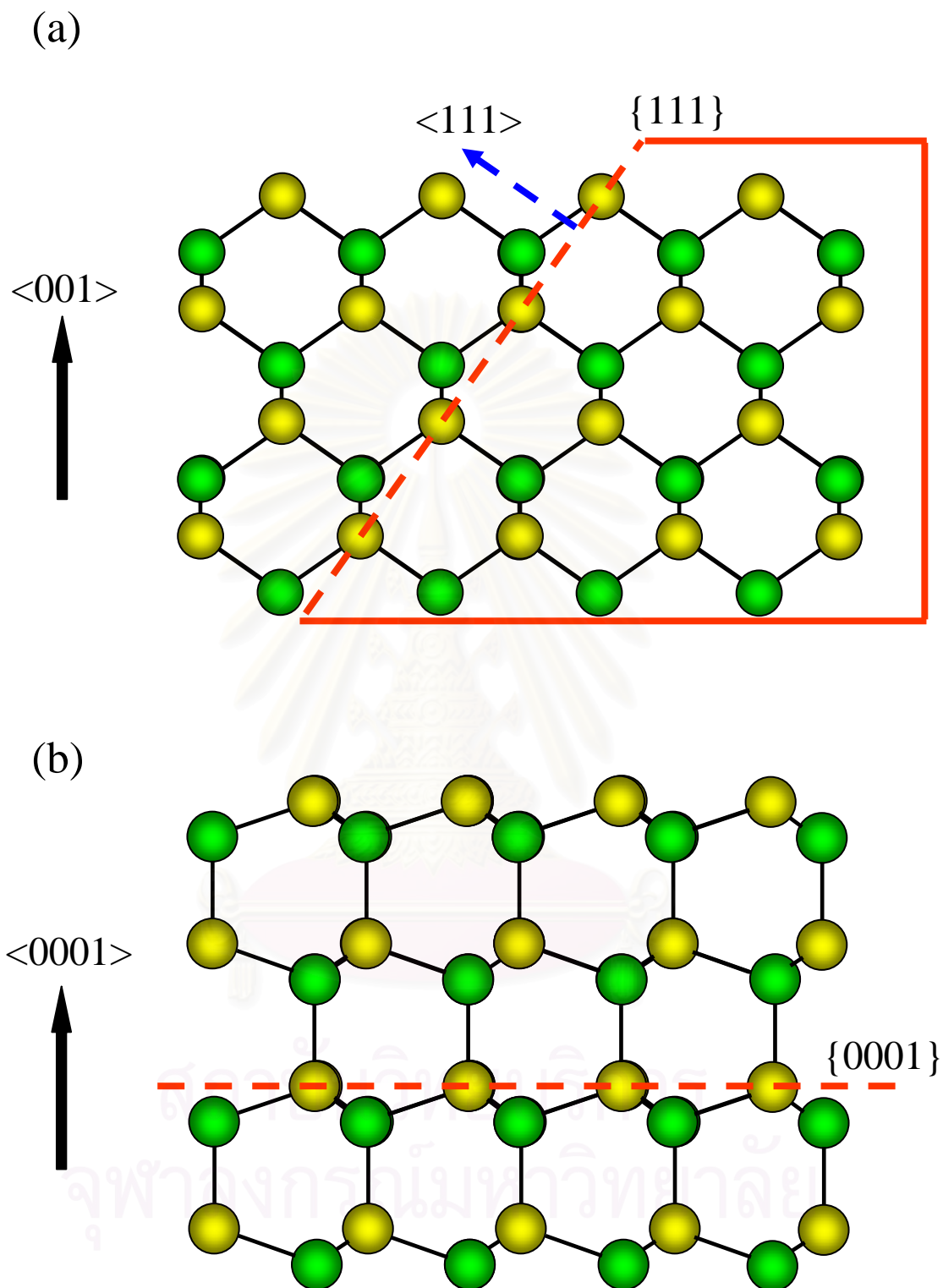


Figure 1.3: Two-dimensional atomic models of crystal structure for InN along (-110) cross-section, (a) cubic structure and (b) hexagonal structure [32]

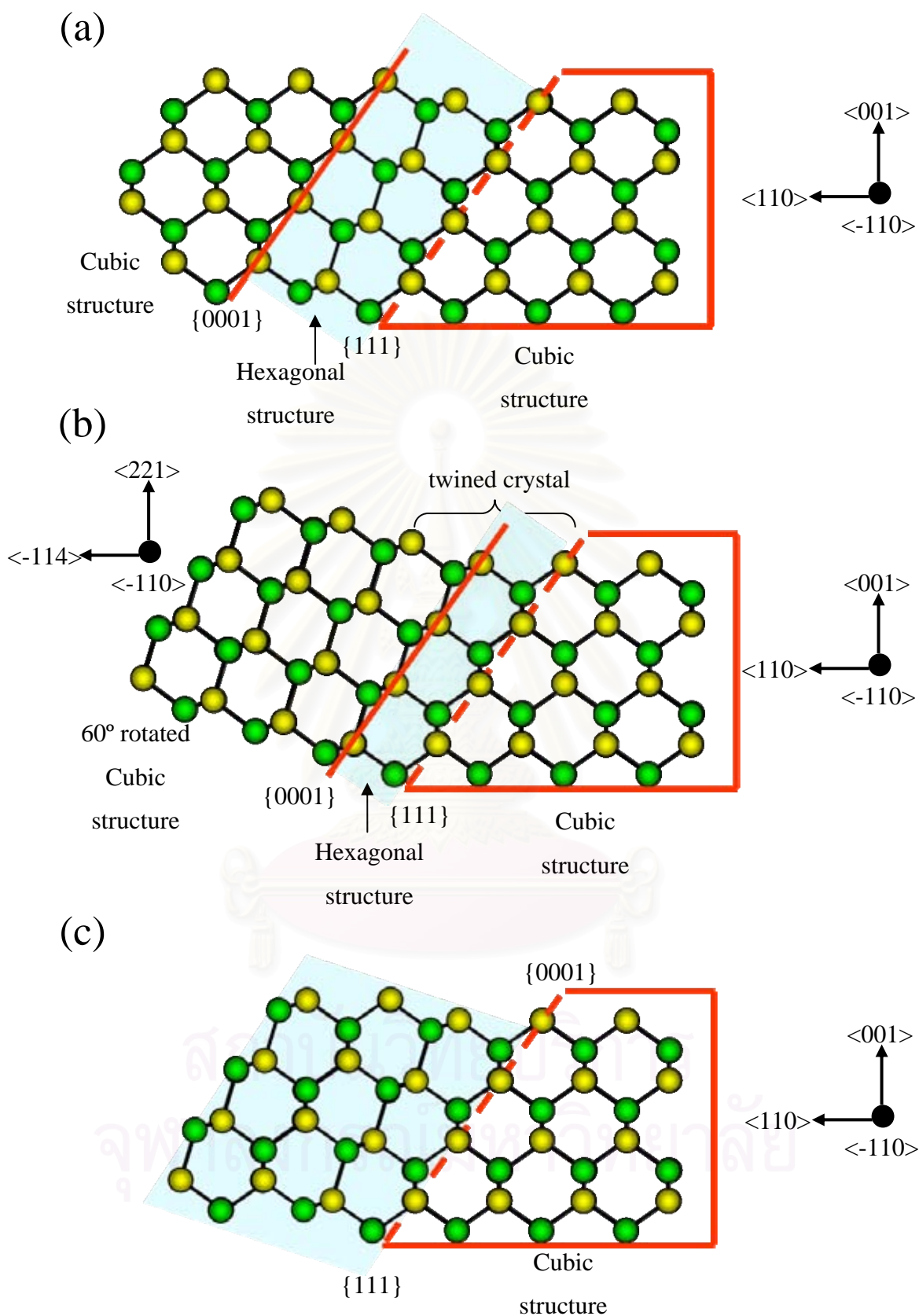


Figure 1.4: Schematic illustration of possible of planar defects in *c*-InN film along $\langle -110 \rangle$ cross-section, (a) stacking faults, (b) twins and (c) hexagonal phase subdomain [32]

1.3 Objectives and organization of the thesis

The aim of the thesis is to investigate and analyze major defects presented in *c*-InN films grown on GaAs (001) substrates by MBE. The effects of In- and N-rich growth condition on micro-structural in *c*-InN films were investigated. Micro-structural properties of the *c*-InN films were investigated using high-resolution X-ray diffraction (HRXRD), Raman scattering and transmission electron microscopy (TEM).

The thesis is organized as follows:

Chapter II: In this chapter, we introduce an epitaxy growth, strain and defects in epilayer. The basic principles of characterization techniques, including HRXRD, Raman scattering and TEM are described.

Chapter III: In this chapter, we describe the experimental procedure and details of the *c*-InN films used in this study. In addition, the sample preparation of the TEM observation is described in details.

Chapter IV: Initial investigational results, such as surface morphology, crystal structure and correlation between vibration properties in the *c*-InN layers, are given and discussed. To investigate the effects of growth conditions (In- and N-rich condition) we also focus on the TEM results, especially crystal structure, epitaxial relationship and defect structures in the *c*-InN grown layer.

Finally, Chapter V gives the conclusions of the thesis.

CHAPTER II

STRUCTURAL PROPERTIES AND CHARACTERIZATION

In this chapter, we introduce the epitaxial growth and structural defect generated in an epitaxial layer. Then after, the investigation methods of lattice constants, crystal structure and structural defects, i. e. high resolution X-ray diffraction (HRXRD), Raman scattering and transmission electron microscopy (TEM) techniques, are described in details.

2.1 Epitaxial growth

Epitaxy is a term used to describe an extended single-crystal film formation on top of a crystalline substrate. The deposited film can be denoted by the terminologies such as epitaxial layer or epilayer. There are two type of epitaxy. The first type is homoepitaxy referring to the case where the film and substrate are the same material. The second type is heteroepitaxy referring to the case where the film and substrate are different materials. It is well known that optoelectronic devices, such as light-emitting diodes (LEDs) and laser diodes (LDs), use the compound semiconductors in form of heteroepitaxial film structures [22], which can be explained using three possible models of heteroepitaxial structures, as shown in Fig. 2.1.

2.2 Strain relaxation

Figure 2.1(a) shows a heteroepitaxial layer “called epilayer”, which is grown on a crystalline substrate with the same crystal structure and lattice constant. In this case, the epilayer with an arbitrary thickness can be grown without any defect formation, such as dislocations and stacking faults (SFs). While, these two materials have the same lattice constant, it is accepted as “lattice-match” with a condition of $a_s = a_o = a_{//} = a_{\perp}$. Here, a_s is the lattice constant of the substrate; a_o is the free

lattice constant of the epilayer; $a_{//}$ is the lattice constant parallel to the surface of the substrate; and a_{\perp} is the lattice constant perpendicular to the surface of the substrate. Addition, the heterojunction interfacial structure is essentially like that for homoepitaxial structure.

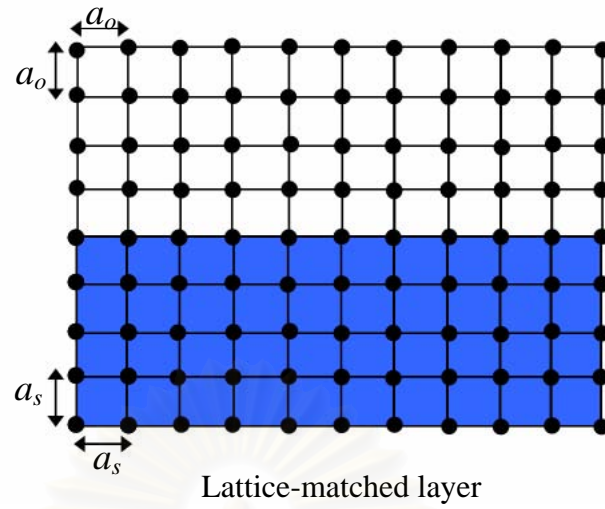
In Fig. 2.1(b), an epilayer grown on a substrate, which has a different lattice constant ($a_s \neq a_o$), results in a lattice-mismatch. In this case, the lattice-mismatched layer is under a tensile strain condition ($a_{//} = a_s, a_{//} > a_{\perp}$). If the lattice constant of layer is larger than of the substrate, the epilayer is under a compressive strain condition ($a_{//} = a_s, a_{//} < a_{\perp}$).

Figure 2.1(c) show the epilayer is grown on a substrate with a different crystal structure and lattice constant, that is, $a_s \neq a_o$. In this case, an epilayer of which thickness is greater than its critical thickness relaxes in order to reduce the strain in the layer, where $a_{//} = a_{\perp} = a_o$.

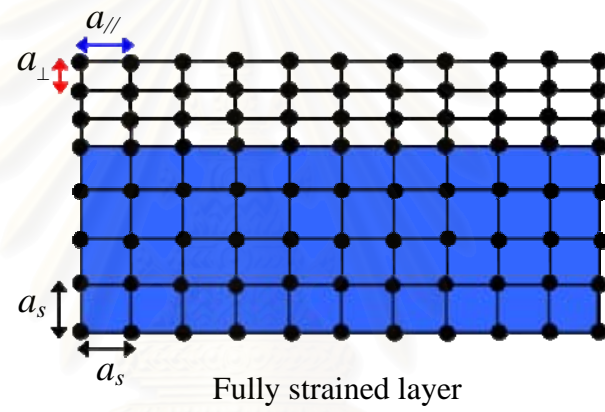
In fact, an effect of strain relaxed is a generation crystal defect, such as dislocations, stacking faults and twins.

2.3 Generation of defects in epitaxial films

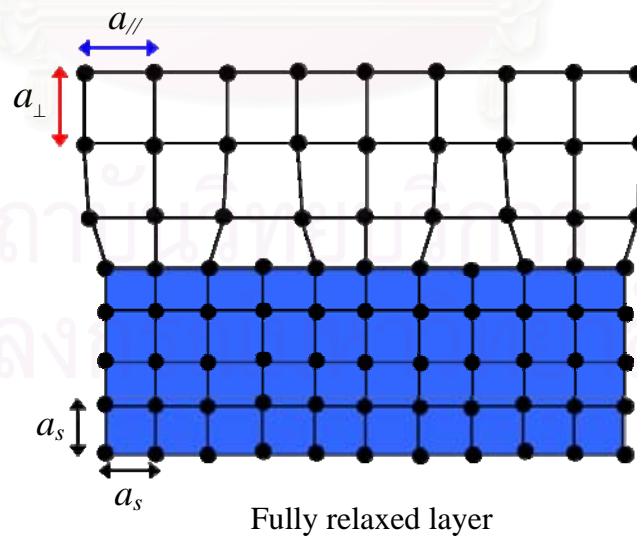
In a perfectly crystal the atom are arrange in a pattern the space lattice. Most crystalline material is not perfect. The regular pattern of atomic arrangement is interrupted by crystal defects. Generally defects in crystalline structures can be classified according to their dimension which defined as imperfections and mistakes in regular periodic arrangement of atom [23]. For 0-dimension defects or point defects which there are two type of point defect, including vacancies and interstitials. Vacancy is simply an unoccupied atom site in crystal structure. The intestinal or interstitialcy is an atom occupying an interstitial site not normal by an atom in perfect crystal structure or extra atom inserted into the perfect crystal. For 1-dimension defects or line defects, such as a curve or straight line which these defects are called dislocations, are created when plane of atoms are distorted out of their regular position. For 2-dimension defects or planar defects which consist of stacking fault, grain boundaries and twin boundaries etc. A stacking fault is local planar of atom



(a)



(b)



(c)

Figure 2.1: Schematic illustration of (a) lattice-matched layer, (b) fully strained layer and (c) fully relaxed layer heteroepitaxial structures [22]

region in the crystal lattice where the regular sequence is interrupted. This is formed either by removal or insertion of plane. The insertion of an extra plane in the stacking is known as an extrinsic stacking fault, while the removal of plane is referred to as an intrinsic stacking fault. Stacking fault is best describe by stacking sequence of the close-packed plane in face-centre cubic structure along the [111] direction or hexagonal structure along the [0001] direction. For example, the stacking sequence of plane in face-centre cubic structure is *ABCABCABC...*. If local stacking sequence is changed into *ABCBCABC...*, this is formed by intrinsic stacking fault. A grain boundary refers to the transition or interface between crystals whose atomic arrangements are different in orientation with respect to each other. A twin is planar defect where a mirror image of the regular lattice is formed during the growth. The twin boundary is the mirror plane of the twin formation. The last type of defect is 3-dimensional or bulk defect which include voids and precipitates. Voids are small areas where there are no atoms and can be thought of as clusters of vacancies. Impurities can cluster together to form small regions of a different phase. These are often called precipitates. The crystal defects have important effects on the properties of the crystalline materials.

2.4 Structural characterization

A brief description of high resolution X-ray diffraction (HRXRD), Raman scattering and transmission electron microscopy (TEM) techniques are given in the following sections.

2.4.1 High-resolution X-ray diffraction

High resolution X-Ray diffraction (HRXRD) is a tool which allows performing structural analysis of crystal materials. Most semiconductor film structures are epitaxially grown on a substrate wafer. These films are nearly-perfect crystalline structures and low defect density. The properties of these films are largely determined by their composition and crystal structure. Information from these layers, such as lattice constants, crystal structure, strain and relaxation, these can be obtained by measuring rocking curves and reciprocal space maps using HRXRD.

In this work, we focus on lattice constant and crystal structure are investigated by measuring rocking curves

When parallel X-rays strike a pair of parallel lattice planes, every atom within the planes acts as a scattering center and reflects a secondary wave, as shown in Fig. 2.2. All of the secondary waves combine to form a reflected wave. The same occurs on the parallel lattice planes with the lattice plane distance of d_{hkl} . All these reflected waves interfere with each other and obey Bragg's law.

$$2d \sin \theta = n\lambda . \quad (2.1)$$

HRXRD technique is used to determine lattice constants (a_{\perp} and a_{\parallel}) of the epilayer, which correspond to the lattice constant perpendicular to the substrate and the lattice constant parallel to the surface of the substrate, respectively. Values of the lattice constant can be obtained from the symmetric (002) $2\theta/\omega$ -scan and asymmetric reflection (113) mapping between the ω -scan and $2\theta/\omega$ -scan modes, which is called "reciprocal lattice space mapping (RSM)".

The first, the symmetric reflect (002) $2\theta/\omega$ -scan was measured to determine the value of interplanar spacing (d_{hkl}). Thus, the value of d_{hkl} in tetragonal system can be represented as follow,

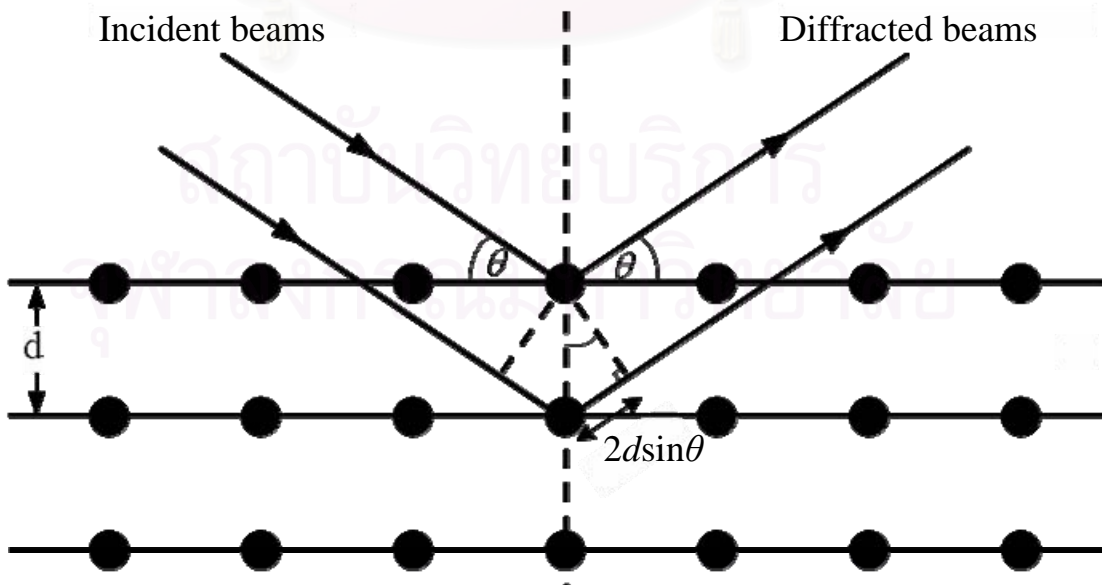


Figure 2.2: Schematic diagram of Bragg's law

$$d_{hkl} = \frac{a_{//}}{\sqrt{h^2 + k^2}} + \frac{a_{\perp}}{l^2}. \quad (2.2)$$

After that, we can obtain value of a_{\perp} from interplanar spacing $d_{002} = a_{\perp}/2$, which is measured using (002) $2\theta/\omega$ -scan mode. Therefore, we can make a combination between equations (2.1) and (2.2); thus, we obtain

$$a_{\perp} = \frac{\lambda}{\sin \theta}. \quad (2.3)$$

The second, the asymmetric reflection (113) mapping between ω -scan and $2\theta/\omega$ -scan modes, which is known as a “reciprocal space mapping” is analyzed to determine the value of $a_{//}$ of the epilayers.

2.4.2 Raman scattering

When the monochromatic high frequency laser light is incident on the sample, the frequency of the scattered light differs from that of the incident light by the frequency of an optical phonon, the scattering process is called Raman scattering. Inelastic scattering of light by molecular vibrations was first reported by Chandrasekhara Venkata Raman. In 1930 Raman was awarded the Nobel prize for his discovery of Raman scattering. In Raman scattering, the incident light beam is scattered with relatively large frequency shift independent of the scattering angle. The Raman spectrum has Stokes and anti-Stokes branches corresponding to the emission and absorption, respectively. The interaction shown in Figs. 2.3(a) and 2.3(b) is Stokes and anti-Stokes process, respectively. Mostly Stokes scattering is used. Conservation of energy and momentum during the interaction requires that

$$\omega_i = \omega_s \pm \omega, \quad (2.4)$$

$$\vec{k}_i = \vec{k}_s \pm \vec{k}, \quad (2.5)$$

where ω_i and \vec{k}_i are frequency and wavevector of the incident photon, respectively. ω_s and \vec{k}_s are frequency and wavevector of the scattered photon, respectively. The +

signs correspond to phonon emission (Stokes scattering), while the – signs correspond to phonon absorption (anti-Stokes scattering). Thus the light is shifted down in frequency during a Stokes process and up in frequency in the anti-Stokes process. The frequency of the phonons can be scattered photons is named as “Raman frequency” or “Raman shift”. Thus the main use of inelastic light scattering is to measure phonon frequencies.

The scattering geometry is commonly written as $\vec{k}_i(e_i, e_s)\vec{k}_s$, which is so called Portó notation [24]; where \vec{k}_i and \vec{k}_s are the directions of incident and scattered photons; e_i and e_s are the polarizations of incident and scattered photons, respectively. The simplest scattering geometry is the backscattering. From the conservation of wavevector, the wavevector \vec{k} of the phonon must be along the [001] direction also for backscattering from a (001) surface of cubic crystal. The longitudinal optical (LO) phonon is polarized in the z direction (or [001] direction), while the transverse optical (TO) phonon is polarized in x-y plane (or (001) plane). Thus, the scattering geometries for backscattering from the (001) surface of cubic crystal are $z(x, y)\bar{z}$ or $z(y, x)\bar{z}$.

The Raman scattering focus is on atomic vibration, wavenumber unit (cm^{-1}) is standard for vibrational studies. Wavenumber is the reciprocal of the wavelength of the light. Since the phonon frequency is equal to the difference between the incident photon frequency and the scattered photon frequency, this difference is referred to as the Raman frequency or Raman shift. Raman spectra are usually plots of the intensity of the scattered radiation versus the Raman shift in wavenumber unit (cm^{-1}).

Raman spectroscopy is a powerful technique to obtain information on crystal structure through measuring the vibrations of the crystal lattice. Raman spectra provide a sensitive tool for studying the impurity incorporation in such structure and the structural defects etc. [25]. Raman spectroscopy can be used to identify the distribution of the hexagonal and cubic [26-27]. In this work, Raman spectroscopy is used to identify the distribution of the hexagonal and cubic phases in the *c*-InN films grown by MBE. The expected results are summarized in Table 2.1. **For *c*-InN the frequency of the optical phonon is split into LO and TO component [28] associated with the incident phonon. On the other hand, for *h*-InN, the LO and TO phonons are represented as the A_1 (LO) and E_2 (high) phonons, respectively, which are the**

strongest ones among the six Raman-active vibrational modes for backscattering along the c -axis [28].

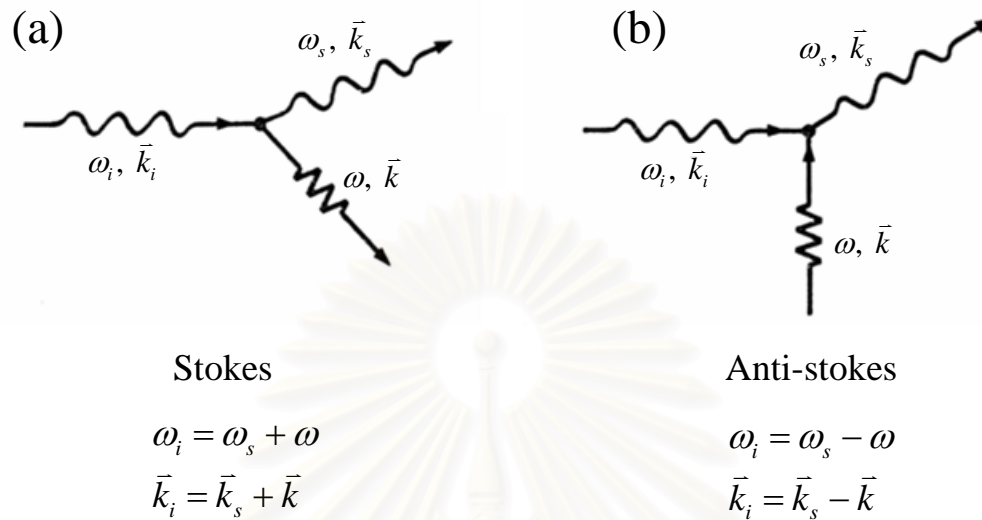


Figure 2.3: Schematic representation of Raman scattering of a photon with (a) emission and (b) absorption of a phonon [35]

Structural phase	Phonon frequencies (cm ⁻¹)			
	E ₂ (high)	A ₁ (LO)	TO	LO
<i>h</i> -InN	488 [28]	586 [28]	-	-
	495 [28]	596 [28]	-	-
	490 [29]	590 [29]	-	-
<i>c</i> -InN	-	-	472 [29]	586 [29]
	-	-	457 [21]	588 [21]
	-	-	467 [21]	596 [21]

Table2.1: Phonon frequencies of InN crystals including both hexagonal and cubic crystal lattices

2.4.2 Transmission electron microscopy

Transmission electron microscopy (TEM) has become a powerful and versatile tool for micro-(nano) structural characterization of crystalline materials because of its ability to observe extended crystal defects, such as dislocations, stacking faults, twins or grain boundaries etc. due to its high spatial resolution capability and high magnification of more than 100,000 times depending on an accelerating voltage [30] and its power to determine the atomic structure of interfaces with a resolution in the order of Angstrom.

2.4.2.1 Principle of TEM system

The TEM operates on the same basic principles as the light microscope but uses electrons instead of light because of limited by the wavelength of light. TEM uses an electron as “light source” and their much lower wavelength makes it possible to get a resolution a thousand times better than with a light microscope. The resolution (d) of a microscope is defined by the smallest distance between two points

$$d = \frac{0.61\lambda}{\mu \sin \beta}. \quad (2.6)$$

Where μ is the refractive index of the viewing medium can be approximated to be the unity; β , the semi-angle of collection of the magnifying lens, is generally very small (a few degrees); and λ , the wavelength of electron beam, is related to the accelerating voltage, V in kV as following

$$\lambda = \frac{1.22}{\sqrt{V}}. \quad (2.7)$$

In TEM, the electron source produced the electron beam energy of typically 100-400 kV. In operation, electrons beam are projected onto the specimen by the condenser lens system is shown in Fig. 2.4. Two condensers lens focus a nearly parallel electron beam onto specimen. The objective, intermediate (first and second) and projector lenses can focus a final magnified image or the diffraction pattern of specimen on the phosphor screen.

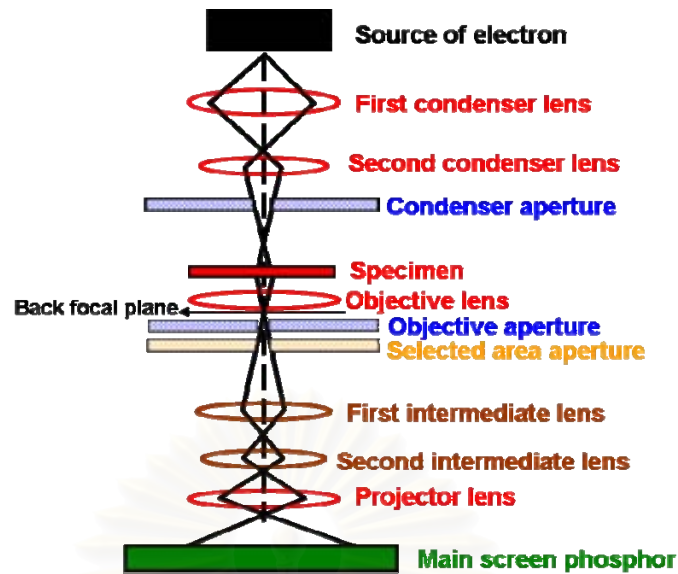


Figure 2.4: Schematic illustration of transmission electron microscopy (TEM) [32, 36]

In the transmitted electron image the crystal structure and defect in solid-state material can be brought into contrast. TEM is classified according to their image formation which there is two modes. A brief description of this image formation will be given in the following sections.

2.4.2.2 Theory of image formation

Image mode

In TEM imaging, the electron diffraction (ED) pattern has to be obtained first, the ED pattern contains bright spots which are associated to the direct transmitted beam and scattered electron beams. Figure 2.5 is the EP pattern from a crystalline material with schematic indication of the location of objective aperture. By selecting either the transmit beam (T) or a diffracted beam (D). When only the transmitted beam is selected, the observation mode is called the bright field (BF) image. On the other hand, when one diffracted beam is selected, it is called the dark field image.

The BF and DF are two basic ways to form amplitude-contrast images. The amplitude contrast (C_A) is defined quantitatively in term of the different

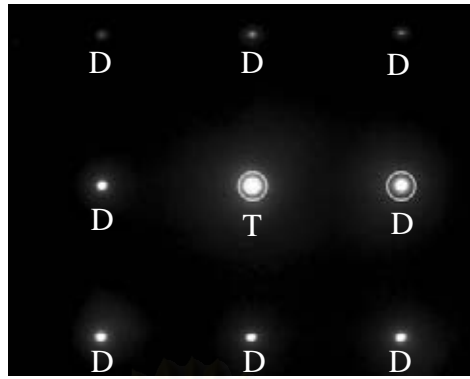


Figure 2.5: Diffraction pattern of diamond silicon showing the relationship between objective apertures and TEM images. The Bright field or Dark field image is formed by selecting the transmit beam (T) or the diffracted beam (D) respectively by using an objective aperture [30, 33]

Intensity (ΔI) two adjacent areas. I_1 and I_2 are intensity of areas 1 and areas 2, respectively.

$$C_A = \frac{I_1 - I_2}{I_2} = \frac{\Delta I}{I_2} \quad (2.8)$$

In fact the contrast in TEM micrograph is seen as different green levels on phosphor screen are formed by coming electron (transmitting and scattering electron) from different thickness, structure and crystal orientation of the specimen. If the contrast in the image were found in some area, it could be primary demonstrated either an appearance of the defect or a difference in orientation of two regions. However, the results must be based on the structural property of material as well as the initial results of previous investigation.

Diffraction mode

The diffraction pattern is formed by the transmitting and diffracting electrons that pass through a thin film and then interfere on the phosphor screen, the arrangement of atoms (structural information) in a specimen can be deduced.

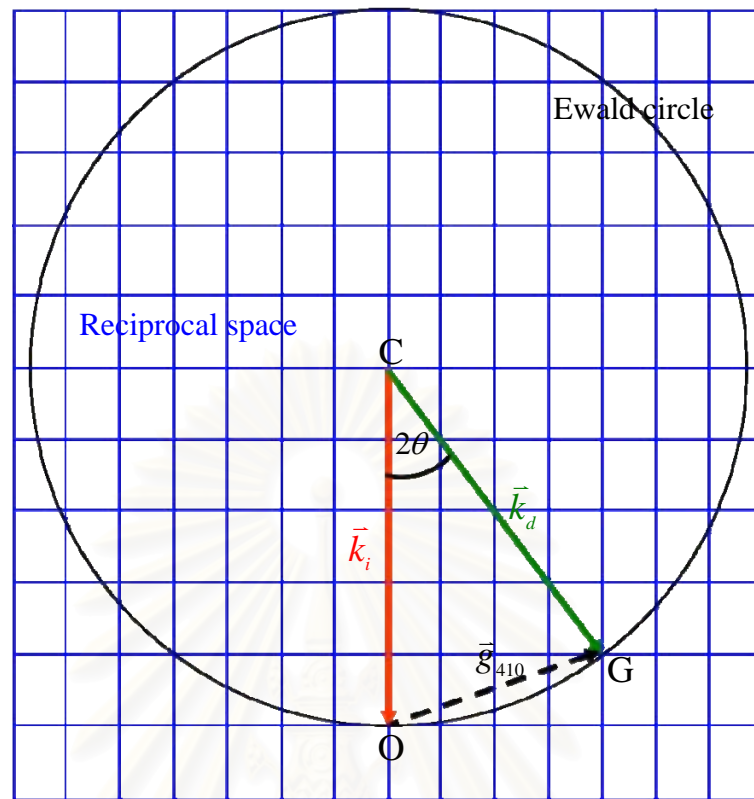


Figure 2.6: Ewald sphere construction in 2 dimensions. Section through the sphere of reflection containing the incident beam vector (\vec{k}_i), the diffraction beam vector (\vec{k}_d) and reciprocal lattice vector (g_{410}) [30, 32]

By using either selected area aperture, a spatial resolution of electron diffraction from several microns to several nanometers can be reached in TEM.

The Ewald constructions

In 1913, Peter Ewald demonstrated the use of the Ewald sphere together with the reciprocal lattice to understand diffraction patterns. It geometrically represents the condition in reciprocal space where the Bragg equation is satisfied.

Consider the incident wave (k_i) falling on the crystal plane has a wave vector \vec{k}_i , as show in Fig. 2.6. The crystal plane is represented by its reciprocal lattice, with origin O. The incident wave is represented by a reciprocal vector \vec{k}_i . Draw the incident wave vector \vec{k}_i , ending at O. Construct a circle with radius $1/\lambda$, which passes

through O. Wherever a reciprocal lattice intersects the circle, Bragg's Law is obeyed and the diffracted electron will occur. CO and CG represent the incident electron and the diffracted electron beam, the corresponding the incident beam vector (\vec{k}_i) and the diffraction beam vector (\vec{k}_d). The angle between them must correspond to Bragg condition (2θ). OG is the \vec{g}_{410} vector, where \vec{g}_{410} is a reciprocal lattice vector, as shown in Figure, $|g_{410}| = 1/d_{410}$ and $|k_i| = |k_d| = 1/\lambda$, thus,

$$OG = 2\left(\frac{1}{\lambda}\right) \sin \theta = \frac{1}{d_{410}}. \quad (2.9)$$

Rearranging this gives Bragg's equation with $n = 1$ will be obtained in equation (2.9).

The reciprocal lattice

The interrelation and indexing of diffraction spots in the diffraction pattern from single crystals are carried using the concept of reciprocal applied originally by Ewald sphere. The reciprocal lattice is constructed from the real lattice by drawing a line through the origin normal to the corresponding reflecting plan of crystal of length equal to the reciprocal of crystal plane spacing. Thus if d_{hkl} is the distance of the (hkl) plane from origin in real space (interplanar spacing), the corresponding distance in reciprocal space is $1/d_{hkl}$. The reciprocal lattice can be constructed as a system of points which will always form a space lattice, e.g., the face centered cubic real lattice has a corresponding body-centered cubic reciprocal is shown in Fig. 2.7. If the reciprocal lattice of unit cell vectors \vec{a}^* , \vec{b}^* , \vec{c}^* are defined in terms of the real space lattice vectors \vec{a} , \vec{b} , \vec{c} , as following

$$\vec{a}^* = \frac{\vec{b} \times \vec{c}}{\vec{a} \cdot (\vec{b} \times \vec{c})}, \quad (2.10)$$

$$\vec{b}^* = \frac{\vec{c} \times \vec{a}}{\vec{b} \cdot (\vec{c} \times \vec{a})}, \quad (2.11)$$

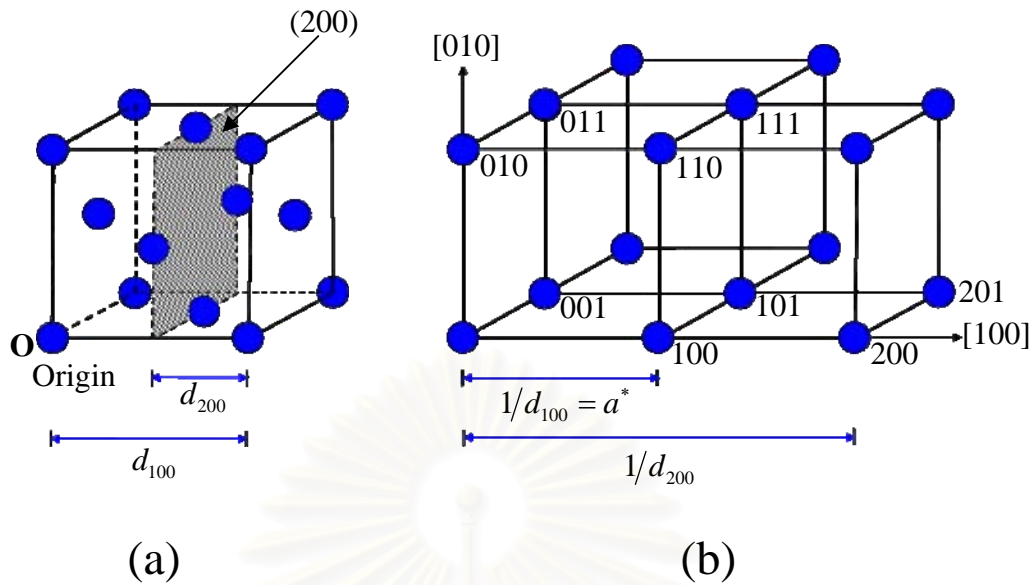


Figure 2.7: The face-centered cubic lattice (a) showing a possible reflecting plane (111) and (b) part of its reciprocal lattice [30, 32]

$$\vec{c}^* = \frac{\vec{a} \times \vec{b}}{\vec{c} \cdot (\vec{a} \times \vec{b})}, \quad (2.12)$$

where, V is the volume of unit cell (i.e., area of base x height). Define the magnitude of the vector as

$$|\vec{a}^*| = \frac{1}{|a|} = \frac{1}{d_{100}}. \quad (2.13)$$

The reciprocal lattice axis $|\vec{a}^*|$ perpendicular to (100) plane of the crystal lattice. Similarly, the reciprocal lattice axes $|\vec{b}^*|$ and $|\vec{c}^*|$ are normal to the (010) and (001) planes of the crystal lattice, respectively. Their magnitudes are equal to the reciprocals of spacing of (010) and (001) planes.

Indexing diffraction patterns

From the diffraction pattern we can get crystallographic information about the crystal such as the lattice constant, orientation relationship of crystal.

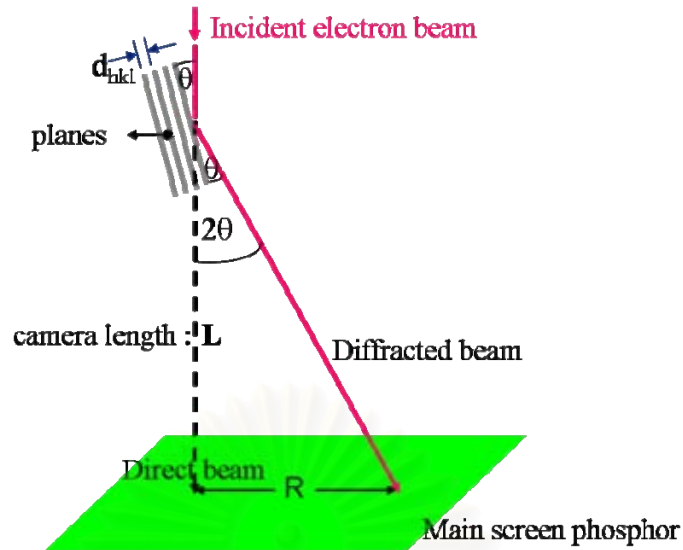


Figure 2.8: Schematic diagram of electron diffraction in TEM [31, 32]

For elastically scattered electrons, the Bragg diffraction law states that

$$2d \sin \theta = n\lambda, \quad (2.14)$$

where d is the interplanar spacing in crystal, λ is the wavelength of the electron beam, θ is the Bragg angle and n can be any integer. In electron diffraction, only first order diffraction, i.e. $n=1$, is considered. In addition, the Bragg angle θ is typically so small that $\sin \theta$ can be approximated by θ . Hence the Bragg equation can be rewritten as

$$2d\theta = \lambda. \quad (2.15)$$

Figure 2.8 is a schematic diagram showing for formation of electron DP in TEM. Thus, a small diffracted angle, $R/L = 2\theta$. Combining with the previous equation, we get

$$\frac{R}{L} = \frac{\lambda}{d} \text{ or } Rd = L\lambda. \quad (2.16)$$

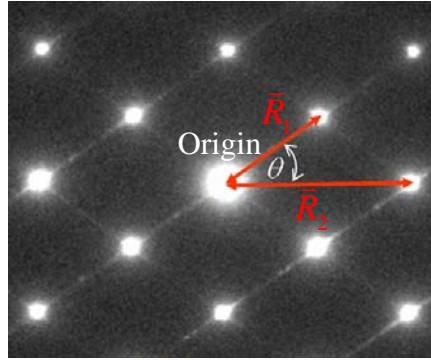


Figure 2.9: Diffraction pattern of InN along [1-10] zone axis

Any distance R , which we measure on diffraction pattern is relate to a specific spacing in the crystal d , then the interplanar spacing d can be determined by measuring R on the diffraction pattern from the origin to diffraction spot as in Fig. 2.9 shows ED pattern of c -InN film grown on GaAs (001) under In-rich growth condition, the corresponding to reciprocal lattice vector (g). Since $L\lambda$ is camera constant, where L is camera length, since it is independent from the specimen the camera length is known. In this case, if the lattice constant for cubic structure can be determined by

$$d = \frac{a}{\sqrt{h^2 + k^2 + l^2}}. \quad (2.17)$$

Thus, combining equation of (2.16) and (2.17), we become

$$\frac{L\lambda}{R} = \frac{a}{\sqrt{h^2 + k^2 + l^2}}, \quad (2.18)$$

where L, λ and a are values of the camera length, the electron wavelength and lattice constant, respective. We can measure several value of R know that

$$R_1 d_1 = R_2 d_2 = R_3 d_3 = R_4 d_4 = \dots \quad (2.19)$$

Therefore the ratio of any two R values gives the ratio of the d -spacing.

		R_1					
R_2	hkl	{111}	{200}	{220}	{311}	{222}	{400}
	{111}	1	1.16	1.63	1.91	2	2.31
	{200}	0.87	1	1.41	1.66	2.45	2.83
	{220}	0.61	0.71	1	1.17	1.22	1.41
	{311}	0.52	0.60	0.85	1	1.04	1.21
	{222}	0.50	0.58	0.82	0.96	1	1.15
	{400}	0.43	0.50	0.71	0.83	0.87	1

Table 2.2: The ratio of d -spacing ratio for some planes of fcc structure [32].

For example, if R_1 is divided by R_2 , as shown in Fig. 2.9, then we will get ratio of the d -spacing any zone axis as following.

$$\frac{R_1}{R_2} = \frac{\sqrt{h_1^2 + k_1^2 + l_1^2}}{\sqrt{h_2^2 + k_2^2 + l_2^2}}. \quad (2.20)$$

Next, we should prepare a table giving the ratio of the d -spacing of permitted diffraction planes on the crystal structure. In this work, we focus on the fcc structure. Then if we know d -spacing ratio taken for the fcc structure were determined and shown in table. For example, the R_1/R_2 ratio determined from measurement of ED pattern in Fig. 2.9 is about 1.63. The two d -spacing ratio shown in Table 2.2 indicates that 1 spot and 2 spot correspond to {220} and {111} planes, respectively.

To confirm these results, the angle between both planes, which have been indexed, is examined using the scalar product, as following

$$\vec{R}_1 \cdot \vec{R}_2 = R_1 R_2 \cos \theta, \quad (2.21)$$

so, for [220] and [111] vectors

$$[220] \cdot [111] = |[220]| \times |[111]| \cos \theta, \quad (2.22)$$

And check with the measured angle, θ in Fig. 2.9. If the measured angle agrees with the calculate angle, the indexing will be accepted. In this case, the measured θ is 35.2° , which the calculated θ is 35.26° . It confirms the results of indexing.

Special case of diffraction patterns

Streaking

Streaking can arise in diffraction patterns because of modifications to the shape of reciprocal lattice points as in arising from either the shape of crystal defect.

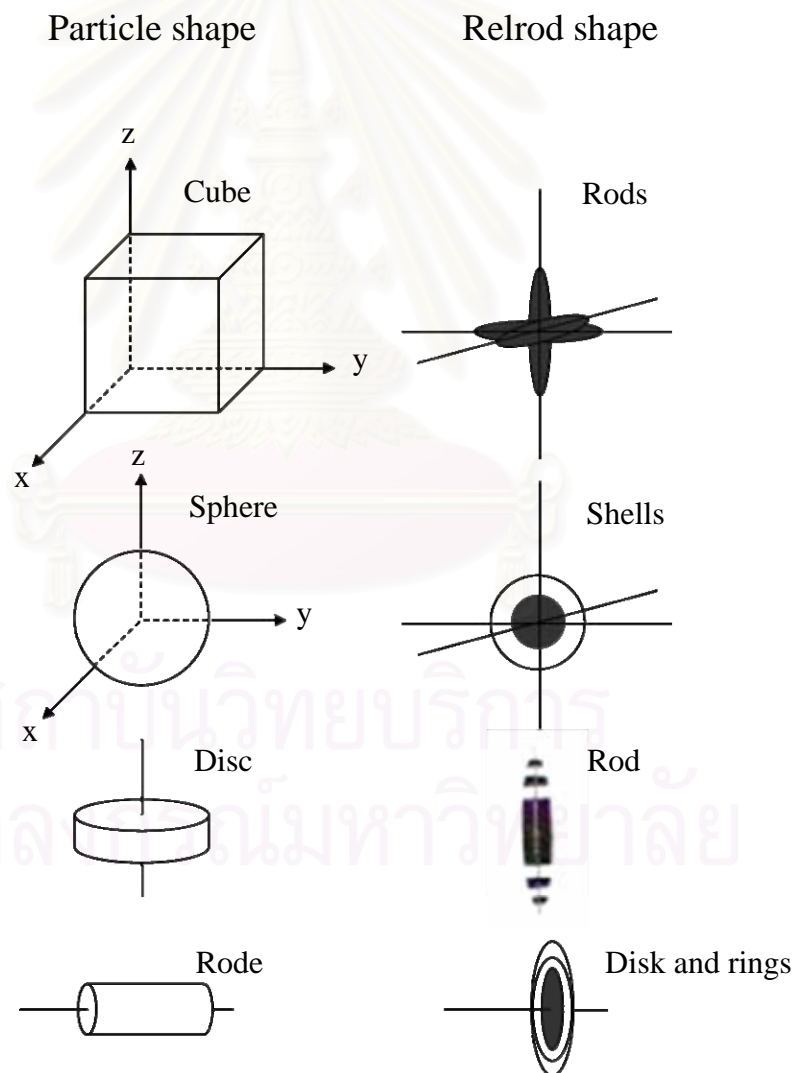


Figure 2.10: Examples of how spots in reciprocal space have different shapes, depending on the shape of the particles which are diffracting [30].

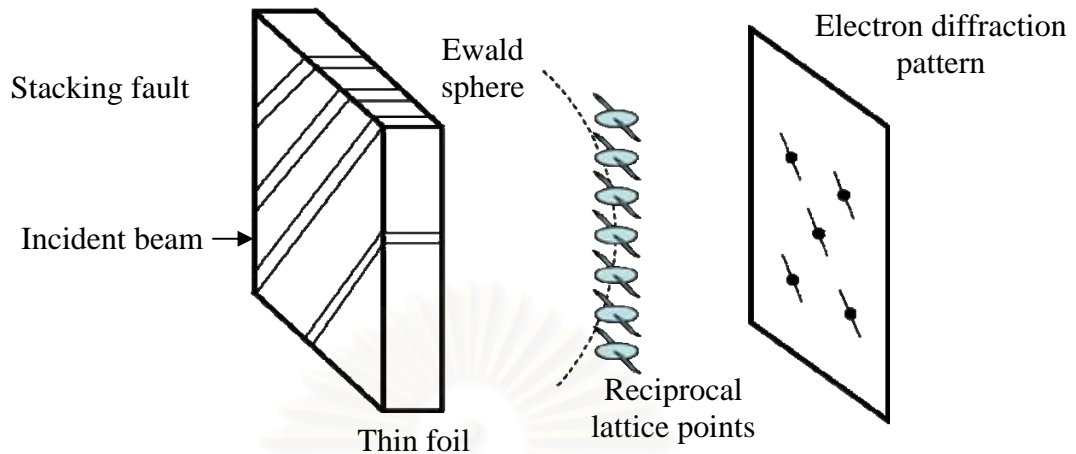


Figure 2.11: Streaking of reciprocal lattice points arising from stacking fault parallel to the electron beam [33].

Streaks are already present in reciprocal space perpendicular to the foil surface running through each reciprocal lattice point. A similar effect is produced if the specimen contains a high density of crystallographically oriented defect such as stacking fault and twin. Origins of the streaks are considered from the intensity distribution at a reciprocal lattice point which arising from specific shapes particle is shown in Fig. 2.10.

On the other hand, the intensity distribution of streaks in the diffraction pattern because the electron diffraction pattern is effectively a section through reciprocal space, the overall effect is to produce either streak. The relationship between a single array of stacking faults normal to the foil surface which the shape of reciprocal lattice point and the diffraction pattern is shown in Fig. 2.11.

CHAPTER III

EXPERIMENTS

In this chapter, we describe the growth information of the *c*-InN films used in this study. Subsequently, sample preparation and experimental setup are shortly explained.

3.1 MBE growth information of *c*-InN films

In this work, all the *c*-InN films were grown on GaAs (001) substrates by molecular beam epitaxy (MBE) system equipped with a radio-frequency nitrogen plasma source, performing at laboratory of Prof. Dr. Kentaro Onabe (Department of Advanced Materials, The University of Tokyo, Japan) [20]. Sample structure of the InN/GaAs is shown in Fig. 3.1. A standard MBE source provided the In flux. A rf-plasma source was used to produce an active N ion. The InN layer was grown at temperature varying in the range of 450-490 °C. The In flux and the rf power were kept constant at 1.5×10^{-4} Pa and 300 W, respectively. To change the V/III ratio, the supplied N₂ flow rate was varied in the range of 1.5 ~ 2.5 standard cubic centimeters per minute (sccm). According to these growth conditions, it is found that the In- and N-rich growth conditions can be controlled by the growth temperature and the supplied N₂ flow rate as well as the V/III ratio.

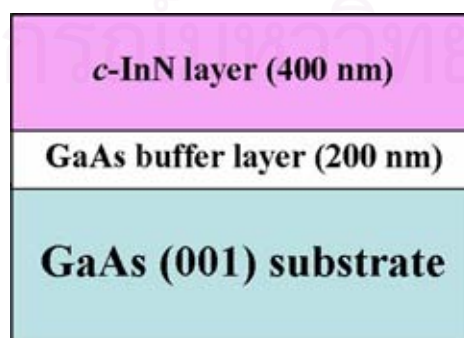


Figure 3.1: Schematic illustration of the *c*- InN film used in this study

3.2 TEM specimen preparation

Specimen preparation is very important an aspect of characterization for TEM. In this work, we focus the preparation method of the cross-sectional specimen is investigated structural defects. The specimen is required to be thin enough for transparent of electrons, obtaining sample of uniform thickness of sample about 200 nm. The cross-section preparation process has four steps which are cutting, clamping, polishing and ion milling steps.

Cutting step

The first step, the specimen surface is cleaned with acetone and methyl alcohol. Next, the surfaces are stuck on a microscope slide with masking tape and are cut the original specimen into small rectangular pieces of $1 \times 2 \text{ mm}^2$ (Fig. 3.2(b)) approximately by diamond-wheel saw, as shown in Fig. 3.2(a). The size of such a small piece is selected to match the specimen grid with 3 mm in diameter, which can be put into the specimen holder in the microscope.

Clamping step

The second step, the surface of cut specimen is cleaned before clamping step. The clamping step is stick surfaces of 2 specimens together with M-BOND 610 glue which is epoxy resin, as shown in Fig. 3.3. After that, the struck specimen is clamped by the clamping holder, as shown in Fig. 3.3(b). The struck specimen in clamping holder is put on the hot plate and heat at temperature about $80 \text{ }^\circ\text{C}$ for 24 hours, as shown in Fig. 3.3(c).

Polishing step

The third step, the clamped specimen is struck on the polishing holder (triangular-shaped glass) with Kenji glue, as shown in Fig. 3.3. The specimen holder is heated on hot plate at temperature about $80 \text{ }^\circ\text{C}$ for 15 minutes, as shown in Fig. 3.3(c). After that, the specimen holder is polished with diamond lapping films on polishing machine with diamond lapping sizes of 9, 6, 3, 1 and $0.5 \text{ }\mu\text{m}$, respectively, as shown in Fig. 3.4, polish until the sample thickness is approximately half of its

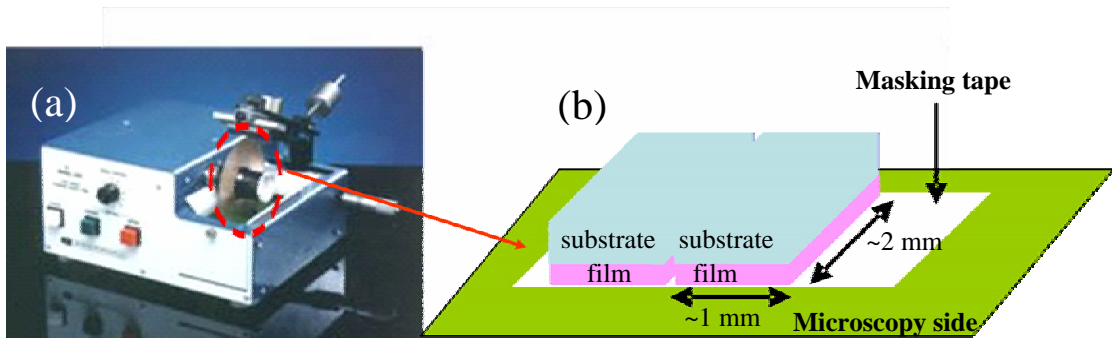


Figure 3.2: (a) Cutting instrument low speed diamond wheel saw, (b) Cut specimen on the microscope slide

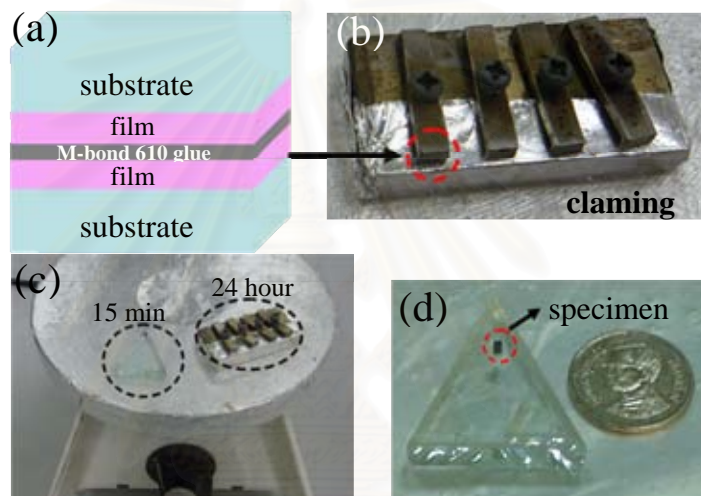


Figure 3.3: (a) Schematic diagram of sticking 2 surface specimens, (b) Clamped specimen, (c) 80 °C for 24 hours heating on the hot plate, (d) Specimen on the triangle glass holder

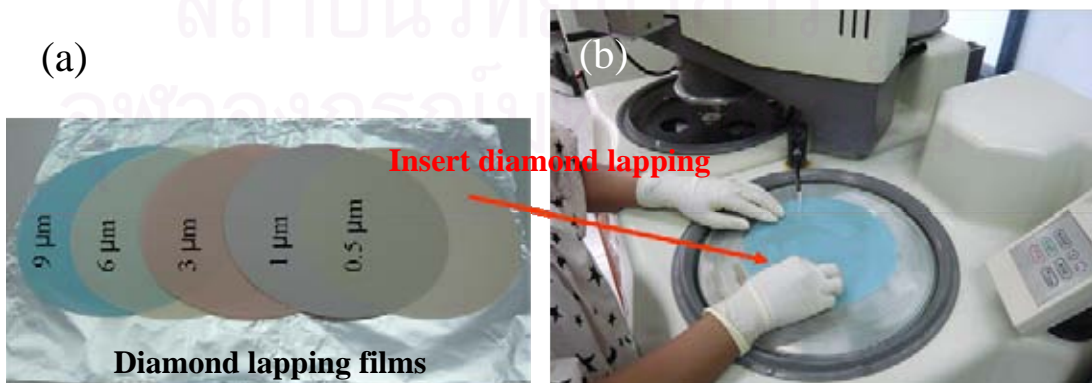


Figure 3.4: (a) Diamond lapping films, (b) Polishing machine



Figure 3.5: Ion beam milling machine

original thickness. The specimen is turned over and polished until the thickness about 50 μm .

Ion milling step

Finally step, the copper grid is stuck on the polished specimen with M-BOND 610 glue. The specimen is heated on the hot plate at temperature about 80 °C for 4 hours. The specimen on copper grid is taken separate from the polishing holder by using acetone. After that, the specimen on copper grid is milled with GATAN Precision Ion Polishing system (PIPs) model 691, which time, voltage and ion beam angle were varied in operate depend on the thickness of specimen, as shown in Fig. 3.5. In this work, the using Ar^+ ions beam with angle about 4° to 10°, 40 keV and time about 5 to 10 minutes. The final thickness of specimen is almost produced for transparent of electrons. Lastly, the grid specimen is put in TEM with a JEOL JEM-2010 microscope, which operated at 200 kV.

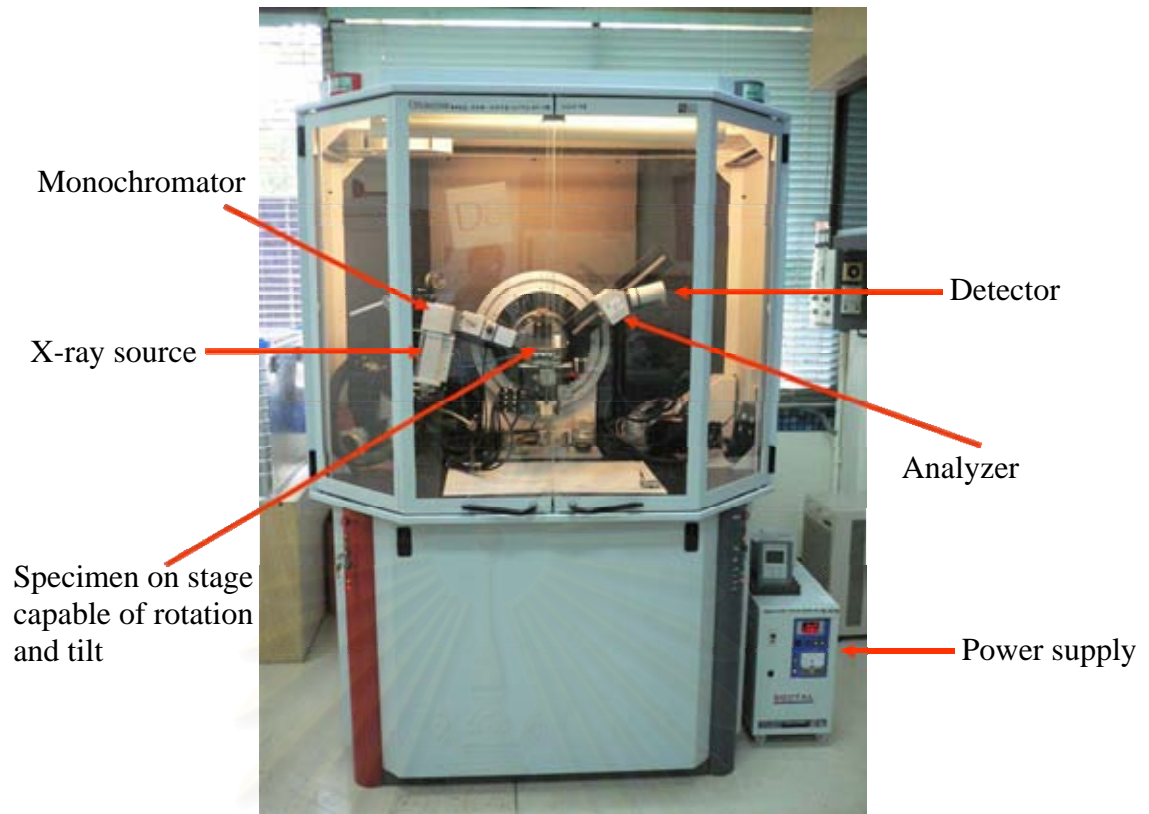


Figure 3.6: Schematic diagram of high-resolution X-ray instrument (Bruker-AXS D8 DISCOVER) at Scientific and Technology Research Equipment Center, Chulalongkorn University

Figure 3.6 shows HRXRD instrument with conventional Cu target operated at 40 kV and 40 mA. The $\text{CuK}\alpha$ radiation is monochromatized into $K\alpha_1$ which the incident X-ray wavelength (λ) of 1.5406 \AA is used. HRXRD technique is used to determine a_{\perp} , a_{\parallel} and a_0 which correspond to the lattice constant perpendicular to the substrate, the lattice constant parallel to the surface of the substrate and the free lattice constant of the epilayer, respectively.

On the other hand, micro-Raman scattering used in this study were done with the Renishaw ramanoscope RM1000 at The Gem and Jewelry Institute of Thailand, Faculty of Science, Chulalongkorn University. Figure 3.7 shows the Raman spectroscopy system. Raman spectra were recorded at room temperature in backscattering geometry on the (001) growth surface of samples.

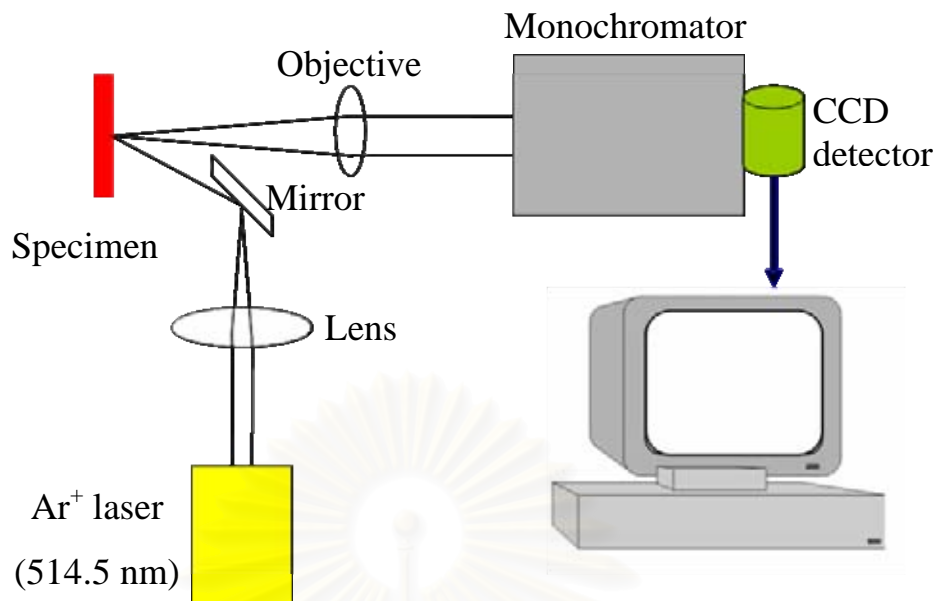


Figure 3.7: Schematic drawing of Raman scattering system

The scattering configuration of $z(x, y)\bar{z}$ is used, where x , y and z correspond to the (100), (010) and (001) crystal directions, respectively. The spectral range was set at the wave number of 250 - 800 cm^{-1} . The Ar^+ 514.5-nm laser line was used as an excitation light source. The excitation laser beam was focused by a microscope lens system yielding a spot size $\sim 2 \mu\text{m}$ in diameter.

สถาบันวิทยบริการ
จุฬาลงกรณ์มหาวิทยาลัย

CHAPTER IV

RESULTS AND DISCUSSION

In this chapter, experimental results of *c*-InN films on GaAs (001) substrates investigated using HRXRD, Raman scattering and TEM are discussed. Formation of structural defects in the studied films grown under In- and N-rich conditions is analyzed. Influence of the growth condition on the generation of structural defects (stacking fault and twin) and single phase *h*-InN in the *c*-InN film is focused.

4.1 Growth information of *c*-InN

c-InN films studied in this study was grown on GaAs (001) substrate by MBE system equipped with a radio-frequency nitrogen plasma source [20]. One-inch GaAs (001) wafer was used as the substrate, and the growth temperature was 450-490 °C. A standard MBE source provides the indium (In) flux. An rf-plasma source was used to produce the active nitrogen flux. The In flux and the rf power were kept constant at 1.5×10^{-4} Pa and 300 W, respectively. The supplied N₂ flow rates were varied 1.5–2.5 sccm.

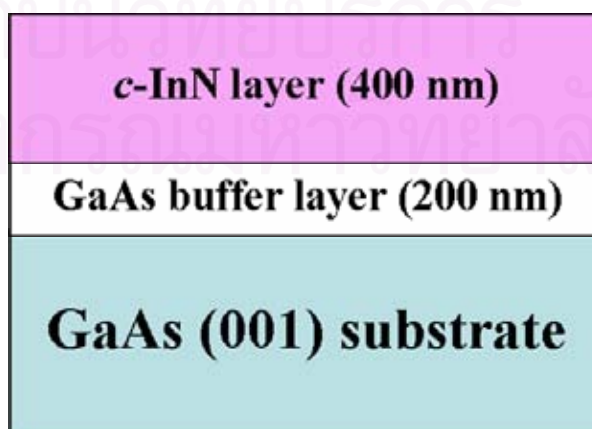


Figure 4.1: Schematic illustration of *c*- InN film grown on GaAs (001) substrate

All the InN layers were grown on the surface of the re-grown GaAs on GaAs (001) substrate for 1 hour. The growth rate was determined to be about 0.4 $\mu\text{m/h}$. The detail of sample structure is shown in Fig. 4.1. The thickness of *c*-InN main layer was determined to be about 300-400 nm depending on growth conditions.

4.2 Identification of growth conditions

The above growth condition of *c*-InN films, it is found that the In- and N-rich growth condition can be controlled by the growth temperature and the supplied N_2 flow rate as well as the V/III ratio [20,34] are summarized in Table 4.1.

The key issue to identify the growth condition is the In droplet [35], which can be seen on the surface for lower supplied N_2 flow rate and higher growth temperatures as shown in Fig. 4.2 (samples A, B and C). An appearance of the In droplets indicates an insufficient V/III ratio, resulting in the In-rich growth condition. On the other hand, the In-droplet-free surface reflects that the growing surface is under the N-rich growth condition as also seen in Fig. 4.2 (samples D, E and F).

To mention the above results, all the samples are selected in order to reach one's objective.

Samples	Temperature (°C)	N_2 flow rate (sccm)	Growth conditions
A	490	1.50	In-rich
B	450	1.50	In-rich
C	490	1.75	In-rich
D	450	1.75	N-rich
E	490	2.25	N-rich
F	450	2.25	N-rich

Table 4.1: Growth conditions for the In- and N-rich of *c*-InN layers [20, 34]

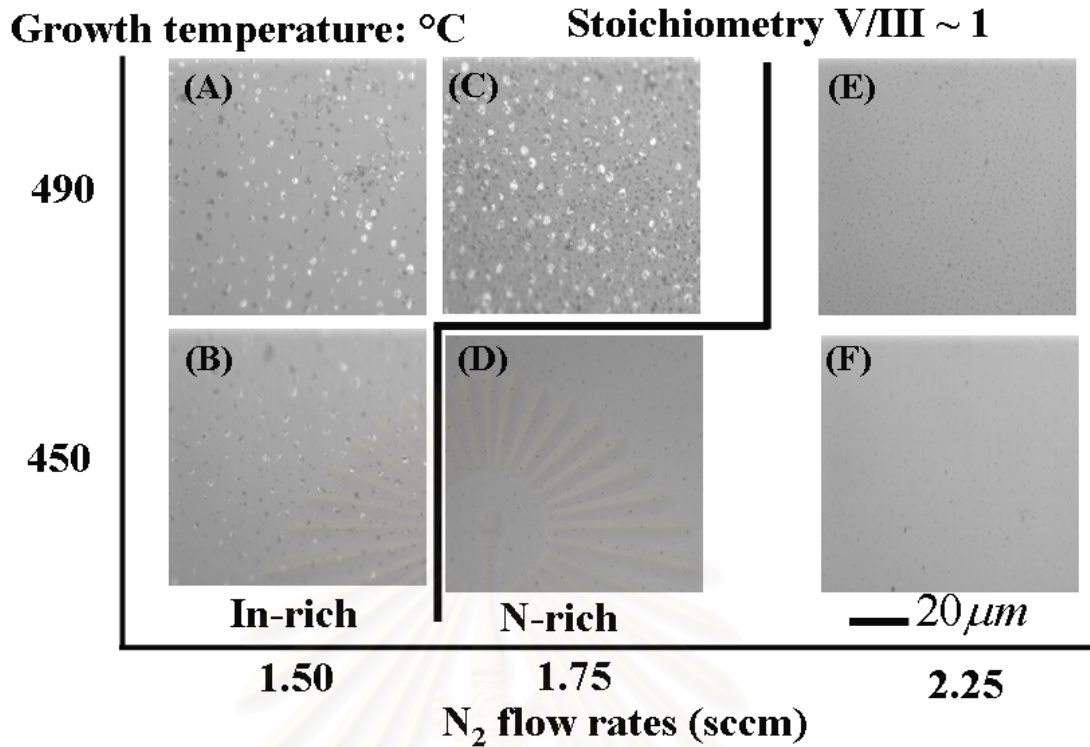


Figure 4.2: Scanning electron microscopy (SEM) image of the *c*-InN grown surfaces at different growth temperatures and supplied N₂ flow rates. White spots in samples A, B and C indicate the In droplets [34]

4.3 Crystal structure of *c*-InN

The crystalline structure was estimated from the $2\theta/\omega$ of HRXRD of (002) diffraction. Figure 4.3 shows the profiles of the *c*-InN films grown on GaAs (001) under In- and N-rich growth conditions. The cubic (002) related diffraction peaks are clearly observed about $2\theta = 36^\circ$, whereas no hexagonal (0002) and (10-11) related diffraction peak were clearly observed about $2\theta = 31.2^\circ$ and $2\theta = 33.1^\circ$, respectively. This clearly demonstrates that all the InN grown films have cubic structure. However, it cannot be concluded that no generation of hexagonal crystal in these *c*-InN layers.

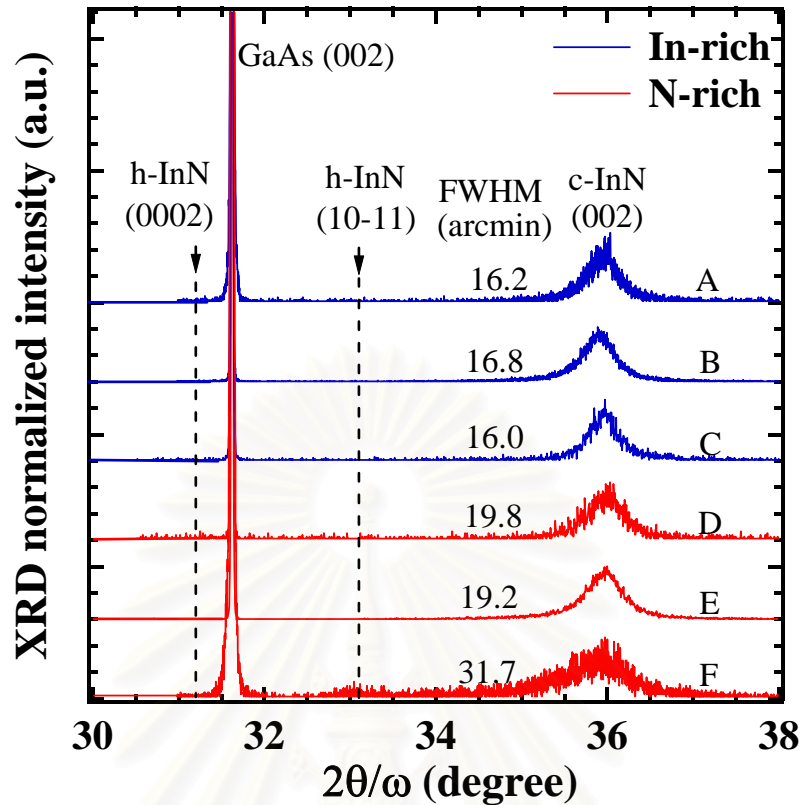


Figure 4.3: $2\theta/\omega$ -scan HRXRD (002) profiles of the *c*-InN films grown on GaAs (001) under In- and N-rich growth condition [34]

4.4 Vibrational properties

In this part, we evaluated the possible impact of the In- and N-rich growth conditions on the vibrational properties in the *c*-InN films using Raman spectroscopy. Figure 4.4 shows Raman spectra of the *c*-InN films on GaAs substrates grown under In-(blue solid curves) and N-(red solid curves) rich growth conditions. The black-dashed and green-dotted lines indicate the characteristic phonon frequencies of cubic and hexagonal structures of the InN crystals [29], respectively. It is found that the cubic LO phonon is clearly observed in the *c*-InN films grown under the In-rich growth condition (samples A, B and C). On the other hand, the *c*-InN films grown under the N-rich growth condition (samples D, E and F), Raman spectra exhibit a mixture of cubic and hexagonal phonon modes. For these films, the A_1 (LO) mode shows broadening and its wide band covering from 550-600 cm^{-1} . In fact, the phonon mode broadening is attributed to structural disorder-activated scattering as that

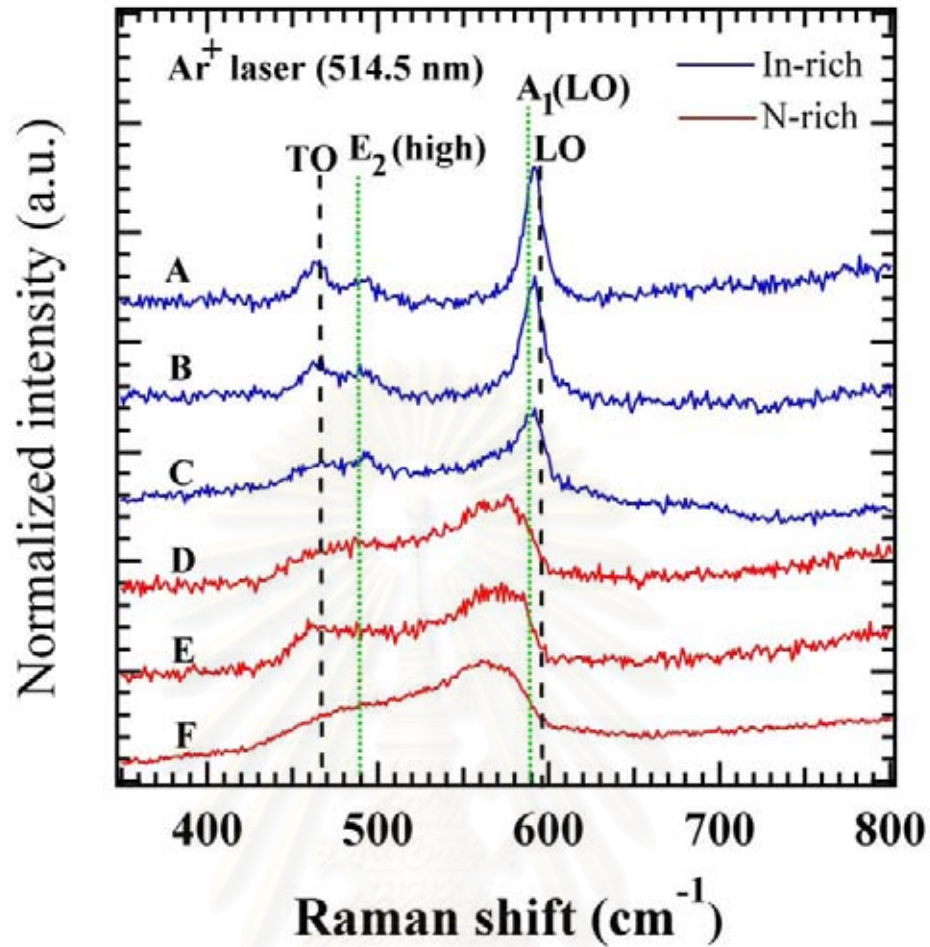


Figure 4.4: Raman spectra of the *c*-InN films grown under In-(blue solid curves) and N-(red-solid curves) rich growth conditions. Black-dashed lines and green-dotted lines indicate the characteristic phonon frequencies of *c*-InN and *h*-InN phases, respectively

observed in other III-N semiconductors. The results demonstrate that the difference in the Raman spectra is in connection with the different amounts of hexagonal phase inclusion in the *c*-InN films [34].

4.5 Morphological investigation of *c*-InN

Figure 4.5 shows cross-section morphology SEM images of the *c*-InN layer grown on GaAs (001) under the In-rich conditions (at 490°C with the N₂ flow rate of

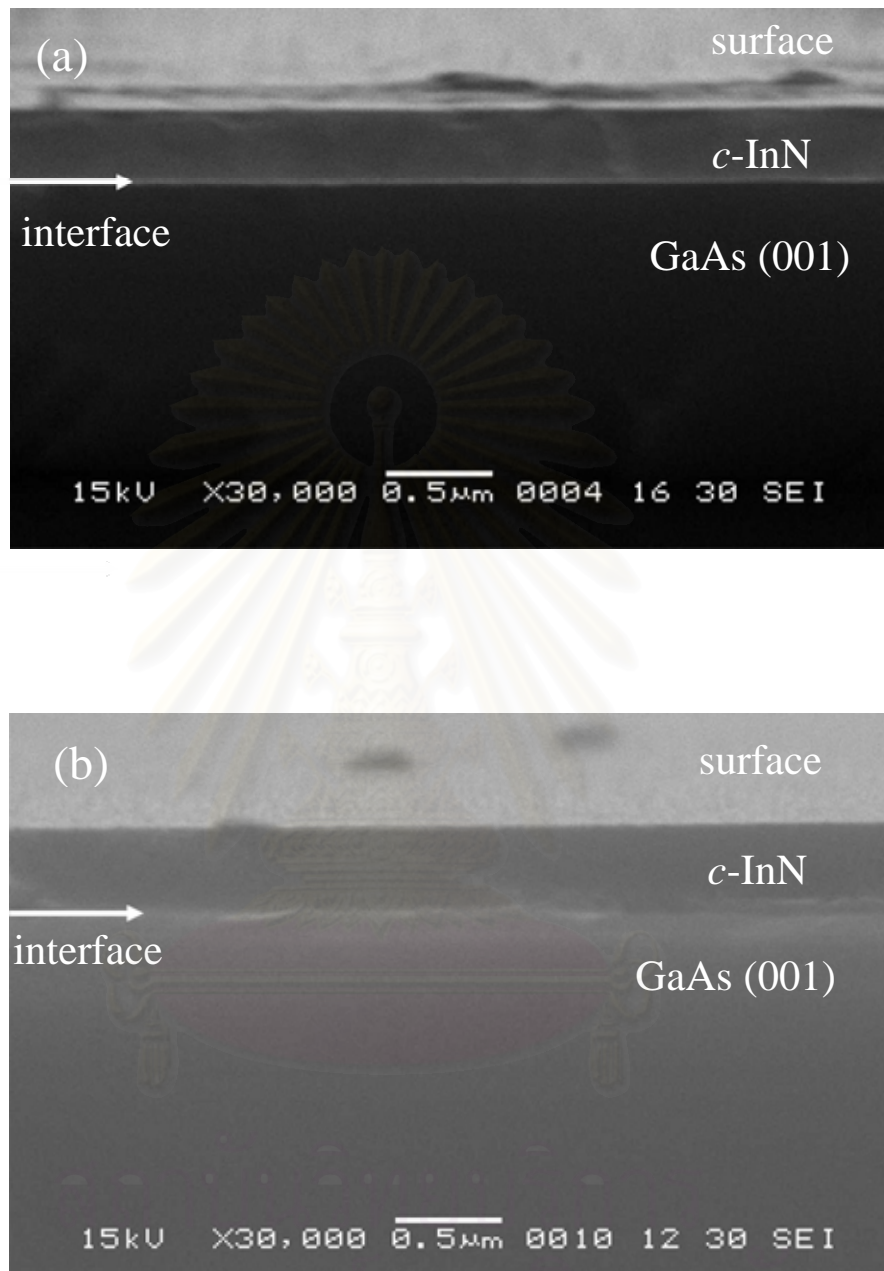


Figure 4.5: Cross-sectional SEM images of the *c*-InN layers grown on GaAs (001) substrate under the In-rich conditions (at 490°C with the N₂ flow rate of 1.50 sccm.) and the N-rich conditions (at 450°C with the N₂ flow rate of 1.75 sccm.), as shown in Figs. 4.5(a) and 4.5(b), respectively

1.50 sccm.) and the N-rich conditions (at 450°C with the N₂ flow rate of 1.75 sccm.).

The interface between *c*-InN layer and the GaAs substrate is fairly flat without generation of any voids. The film thickness was determined to be 350 and 380 nm for In-rich and N-rich layers, respectively.

4.6 Microstructure investigation

Microstructures of epilayer were characterized transmission electron microscopy (TEM). Sample was prepared in cross-section using standard mechanical polishing and ion-milling techniques. TEM was performed at 200 kV in a JEOL JEM-2010 microscope. Figures 4.6(a) and (b) show convention bright field (BF) cross-section TEM image and electron diffraction (ED) pattern of the *c*-InN film on GaAs (001) substrate under the In-rich conditions (at 490°C with the N₂ flow rate of 1.5 sccm). InN layer can be distinguished from substrate by its different contrast. The ED pattern of InN/GaAs (001) interface obtained with the electron beam along the GaAs [1-10] zone axis. The ED pattern consists of spots which round and streaking for GaAs and InN, respectively. In this pattern, the diffraction spots of InN and GaAs are almost superposed for small mismatch of their lattice constants. This pattern indicates that InN has cubic structure type (*c*-InN). Also the orientation relationship between the two sets of diffractions spots of the InN and GaAs shows that exact epitaxial orientation was obtained during growth with the following orientation relationship *c*-InN(001)//GaAs (001) and *c*-InN[1-10]//GaAs [1-10]. The streaks demonstrate the existence of planar defect such as stacking faults (SFs) and twins on {111} plane. The BF cross-section shows line contrasts, which are nearly parallel to {111} in *c*-InN TEM image.

Furthermore, indication of stacking faults originating at the interface and propagating along {111} planes are seen. Double stacking faults leading to appearance of twins can also be observed in InN layers.

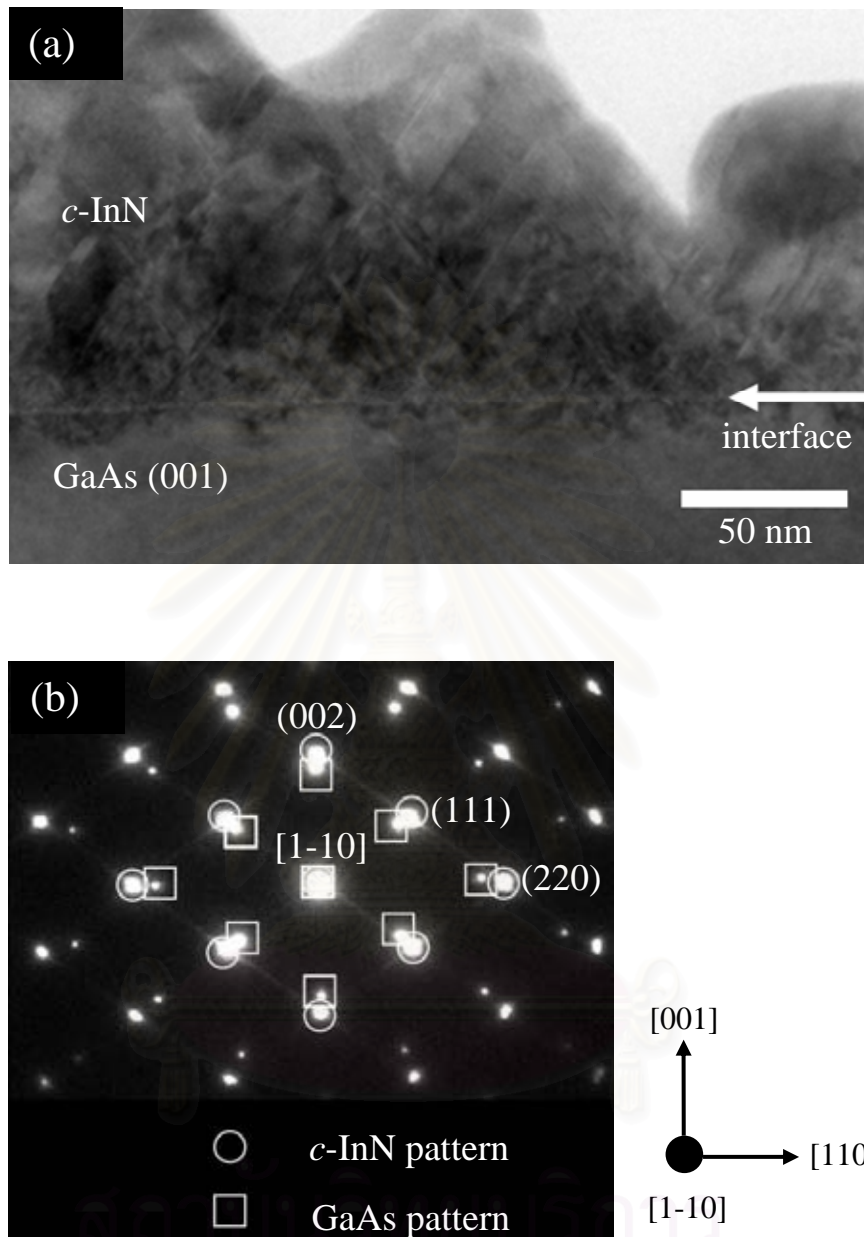


Figure 4.6: (a) Cross-sectional TEM image of *c*-InN film on GaAs (001) substrate grown under the In-rich conditions (at 490°C with the N₂ flow rate of 1.5 sccm) and (b) Electron diffraction patterns taken from the *c*-InN/GaAs region along the [1-10] zone axis

4.7 Effects of In- and N-rich growth conditions

Figure 4.7 shows cross-sectional TEM micrographs for *c*-InN film on GaAs (001) substrate at different growth condition of (a) under the In-rich conditions (at 490°C with the N₂ flow rate of 1.5 sccm) and (c) under the N-rich conditions (at 450°C with the N₂ flow rate of 1.75 sccm). For the In-rich conditions, the ED patterns from the InN layer clearly indicates that the InN grown layer has cubic structure is shown in Fig. 4.7(b). No different type of diffraction spots on the ED pattern was observed. However, the microstructure is characterized by a high density of stacking faults closed the interface and decreased with distance form the InN/GaAs interface (Fig. 4.7(a)), which results in streaking of diffraction spots on the ED pattern (Fig. 4.7(b)). On the other hand, for N-rich growth condition, the ED pattern (Fig. 4.7(d)) shows that the hexagonal phase structure becomes govern in the grown layers. Different type of single diffraction spots marked by arrows related to the hexagonal phase structure. These diffraction spots indicate the incorporation of single-crystal *h*-InN in the *c*-InN layer. Figure 4.7(c) shows that the high density of pyramid-like structures showing (-1-11) and (111) facets and looking like penetrating into the layers are clearly visible at the interface. It is known that an occurrence of a hexagonal-like stacking mode is naturally expected since InN is usually stable in hexagonal structure. These results suggest that SFs, if densely accommodated, can become seeds of the *h*-InN structure in the layer of *c*-InN. These results are agreed well with our previous results obtained from high resolution X-ray diffraction measurements.

Figure 4.8 shows again the ED patterns (the same image as shown in Fig. 4.7(d)). The figure illustrates the observed epitaxial relationship between the *h*-InN and the *c*-InN crystals. The epitaxial relationship between the *c*-InN and hexagonal inclusions was examined to be $c\text{-}\{111\} // h\text{-}(0002)$ and $c\text{-}\langle 1-10 \rangle // h\text{-}\langle 11-20 \rangle$ as illustrated in Fig. 4.8(b),(c) and 4.8(d).

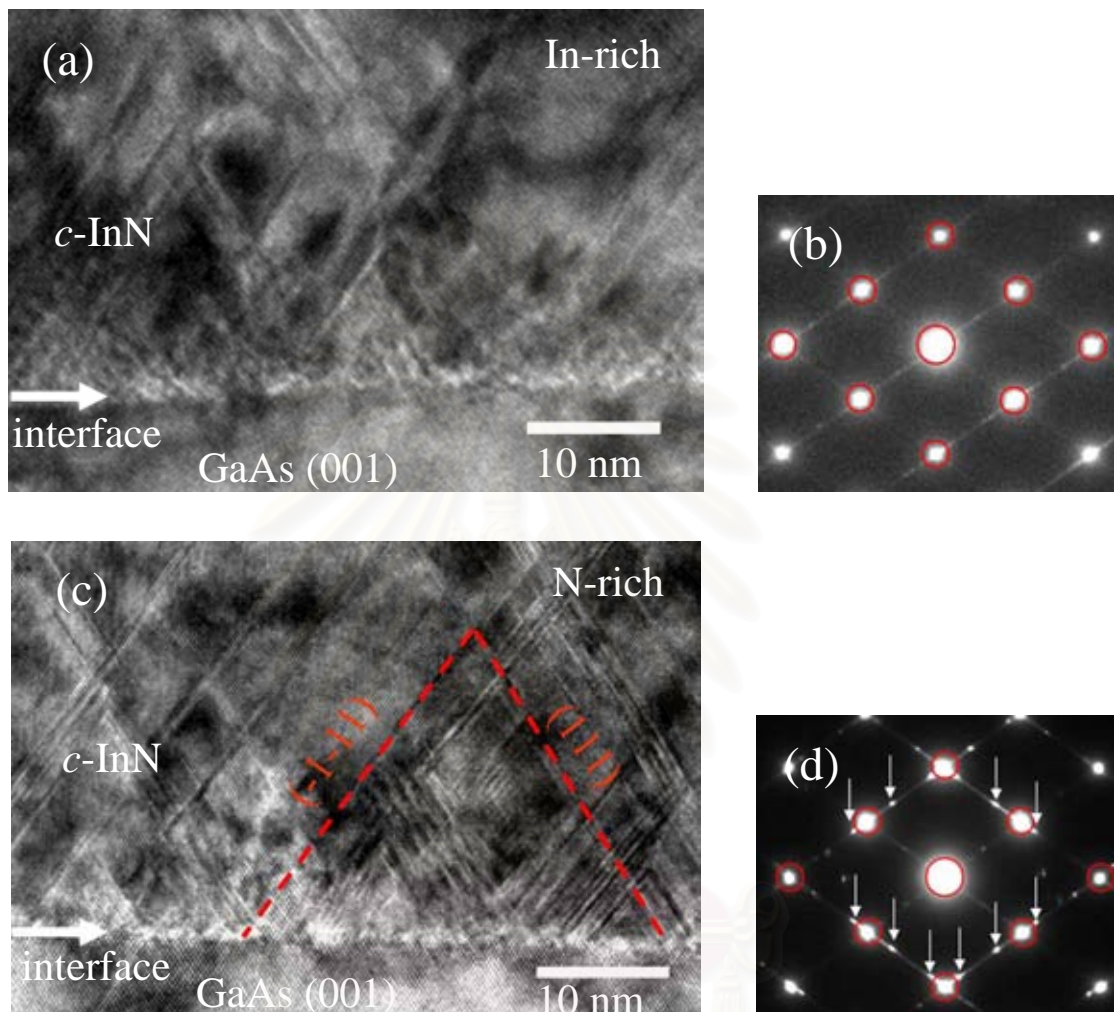


Figure 4.7: (a) Cross-sectional TEM images for *c*-InN film on GaAs (001) substrate at different growth condition of (a) under the In-rich conditions (at 490°C with the N₂ flow rate of 1.5 sccm) and (c) under the N-rich conditions (at 450°C with the N₂ flow rate of 1.75 sccm). (b) and (d) corresponding electron diffraction patterns taken from the *c*-InN region along the [1-10] zone axis of Fig.4.7(a) and 4.7(c), respectively.

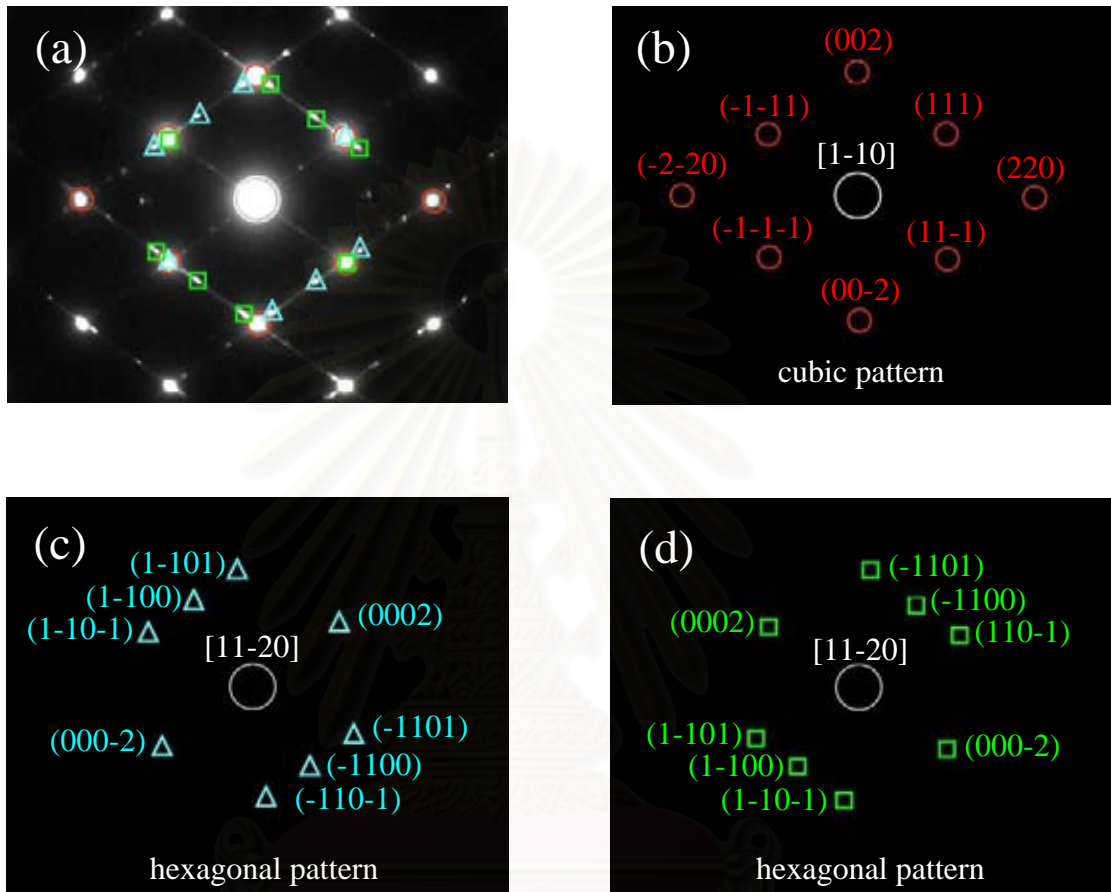


Figure 4.8: (a) Electron diffraction patterns records along the $[1-10]_{c-\text{InN}}$ zone axis from the InN region containing the pyramid-like structures, (b), (c) and (d) show schematic representation cubic and hexagonal phase related diffraction spots, respective

Figure 4.9 shows the dark field cross-sectional TEM images of *c*-InN film on GaAs (001) substrate grown under the In-rich conditions (at 490°C with the N₂ flow rate of 1.5 sccm) which were taken with reflections along *g* vector: (a) *g* = (111), (b) *g* = (002) and (c) *g* = (220) planes. Inset (A), (B) and (C) showing ED patterns were taken from (111), (002) and (220) diffraction spots shown in Fig. 4.9(a), (b) and 4.9(c), respectively. Zone axes is [1-10].

To above the result of *c*-InN films. It is well known that the hexagonal phase is easily generate along (111) cubic plane. In order to verify the existence of stacking faults, the dark field cross-sectional TEM images (Fig. 4.9 (a)) which was taken with reflections along *g* = (111) was used to analyze. As shown in Fig. 4.9 (a), line contrast that was expected to concern the stacking faults is seen clearly. This demonstrates that this line contrast is attributed to stacking faults. Also, the dark field cross-sectional TEM images were used to investigated that the fault plane on (111) plane affect to generation of stacking faults with other plane. Then, we select the (002) and (220) planes to observe the stacking faults. Figure 4.9 (b) and (c) show the dark field cross-sectional TEM images which were taken with reflections along *g* = (002) and (220), respectively. These demonstrate that these line contrasts are attributed to stacking faults.

On the other hand, for N-rich conditions in Fig. 4.10 (at 450°C with the N₂ flow rate of 1.75 sccm.), the dark field cross-sectional TEM images which were taken with reflections along *g* vector: (a) *g* = (111), (b) *g* = (002) and (c) *g* = (220) planes. Inset (A), (B) and (C) showing ED patterns were taken from (111), (002) and (220) diffraction shown in Fig. 4.10(a), (b) and 4.10(c), respective. Zone axes is [1-10] In this case, we describe the result of Fig. 4.10 as the same in Fig 4.9.

In Fig. 4.9 and 4.10 show the dark field cross-sectional TEM images, the bright-contrast regions related to *c*-InN layer. Contrary, the dark-contrast regions related to the *h*-InN subdomains as well as planar defects, i.e. SFs. Also the cross-section the dark field image was used to investigate the existence of high density of stacking fault. In the initial stage of the *c*-InN nucleation under In-and N-rich condition, lots of planar defects (SFs) were formed near the InN/GaAs interface region in the *c*-InN side. But with the progress of the growth, most of the SFs annihilate and *c*-InN grows predominantly. Beside, the higher density of stacking faults is obtained under N-rich than under In- rich growth conditions.

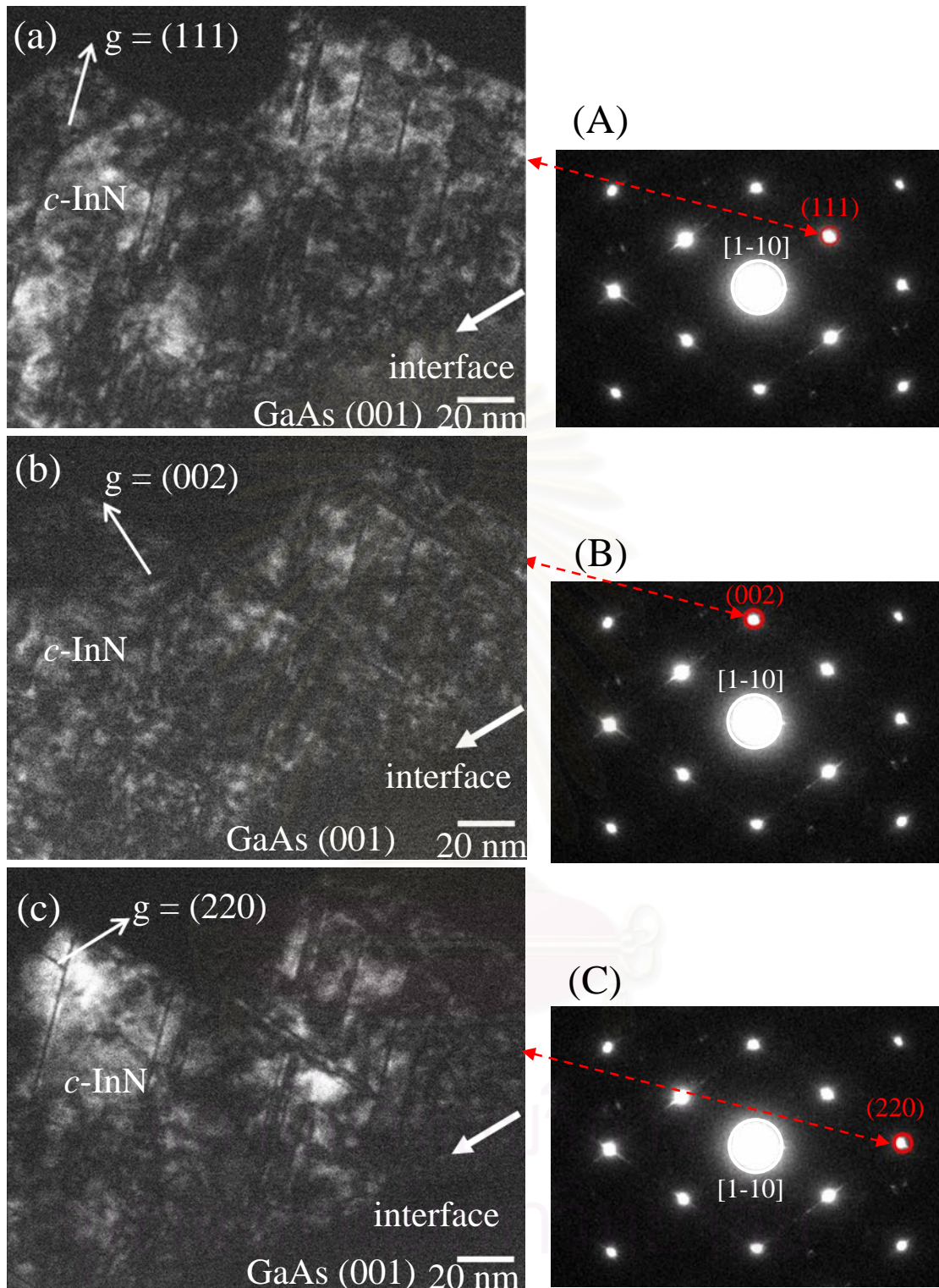


Figure 4.9: Dark field images of *c*-InN film on GaAs (001) substrate grown under the In-rich conditions (at 490°C with the N₂ flow rate of 1.5 sccm) which were taken with reflections along (a) $g = (111)$, (b) $g = (002)$ and (c) $g = (220)$ planes. Inset (A), (B) and (C) showing ED patterns were taken from (111), (002) and (220) diffraction shown in (a), (b) and (c), respective. Zone axes is [1-10]

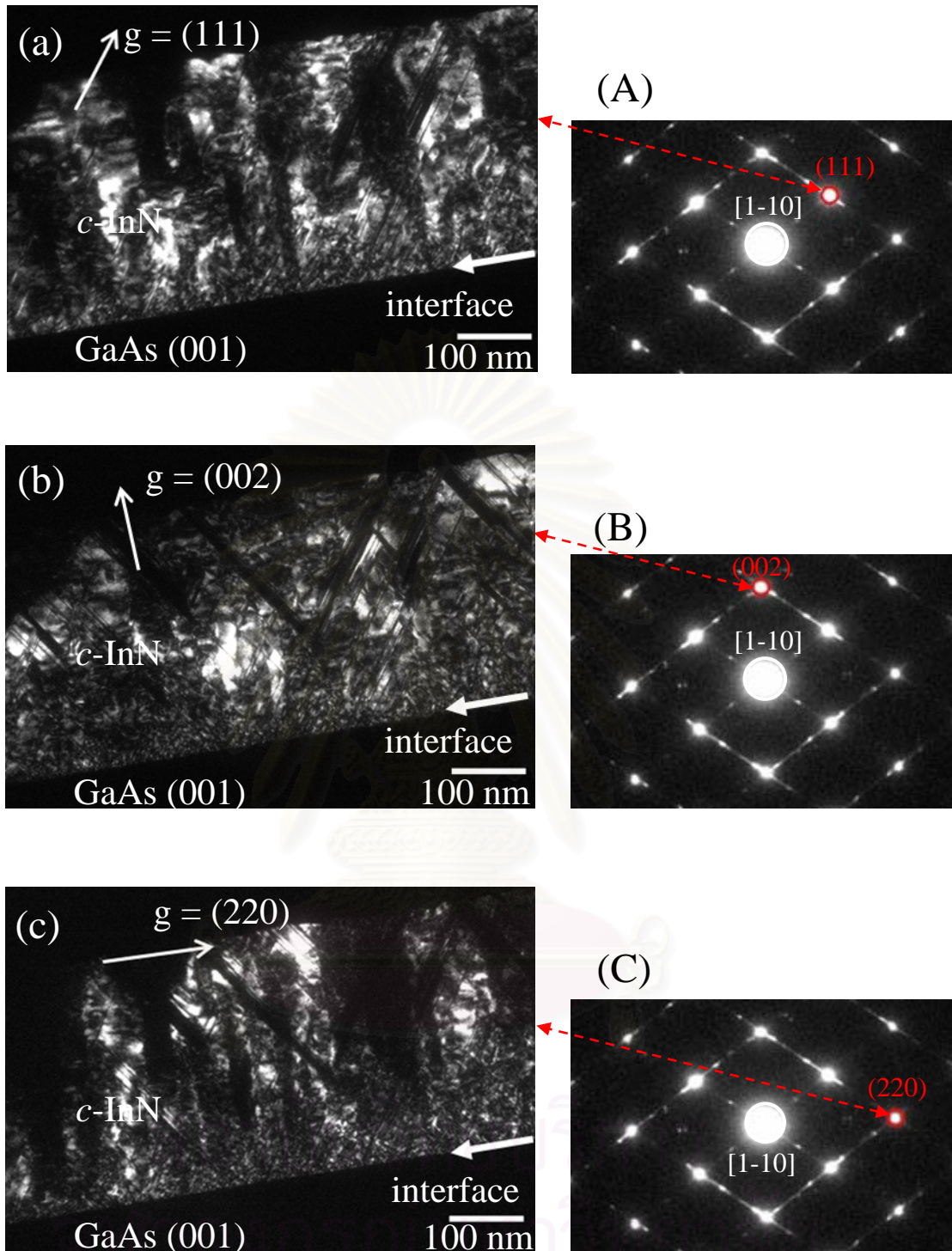


Figure 4.10: Dark field images of $c\text{-InN}$ film on GaAs (001) substrate grown under the N-rich conditions (at 450°C with the N_2 flow rate of 1.75 sccm) which were taken with reflections along (a) $g = (111)$, (b) $g = (002)$ and (c) $g = 220$ planes. Inset (A), (B) and (C) showing ED patterns were taken from (111) , (002) and (220) diffraction shown in (a), (b) and (c), respective. Zone axes is $[1-10]$

On the other hand, In order to verify the existence of the single crystal of hexagonal phase for under In- and N- rich growth conditions, the dark field cross-sectional TEM images which were taken with reflections along g vector: (a) $g = (111)$, (b) $g = (1101)$ and (c) $g = (110-1)$ planes. Inset (A), (B) and (C) showing ED patterns were taken from (111), (1101) and (110-1) diffraction spots shown in Fig. 4.11(a), (b) and 4.11(c), respective. Zone axes is $[1-10]/[11-20]$. The “In-rich” layer in Fig. 4.11(a) shows dark field images which was taken with reflections along $g = (111)$ plane. The bright-contrast region related to c -InN layer. Contrary, the dark-contrast regions within the c -InN layer may relate to the h -InN as well as planar defects, i.e. SFs. In Fig. 4.11(b) and 4.11(c) show dark field images which was taken with reflections along $g = (-1101)$ and (110-1) planes. The bright-contrast regions (Fig. 4.11(b) and 4.11(c)) correspond to the dark-contrast regions in Fig. 4.11(a). The bright-contrast regions at the position marked by red dash circles (Fig. 4.11(b) and 4.11(c)) demonstrate the existence of the single crystal of hexagonal phase. For the N-rich layer in Fig. 4.12 show the dark field cross-sectional TEM images which were taken with reflections along g vector: (a) $g = (111)$, (b) $g = (-1101)$ and (c) $g = (110-1)$ planes. Inset (A), (B) and (C) showing ED patterns were taken from (111), (-1101) and (110-1) diffraction spots shown in Fig.4.12(a), (b) and 4.12(c), respective. Zone axes is $[1-10]/[11-20]$. Figure 4.12(a) shows dark field images which was taken with reflections along $g = (111)$ plane. The bright-contrast region related to c -InN layer. Contrary, the dark-contrast regions within the c -InN layer relate to the h -InN as well as planar defects, i.e. SFs. In Fig. 4.12(b) and 4.12(c) show dark field images which was taken with reflections along $g = (-1101)$ and (110-1) planes. The bright-contrast regions (Fig. 4.12(b) and 4.12(c)) correspond to the dark-contrast regions in Fig. 4.12(a). The bright-contrast regions (Fig. 4.12(b) and 4.12(c)) demonstrate the existence of the single crystal of hexagonal phase.

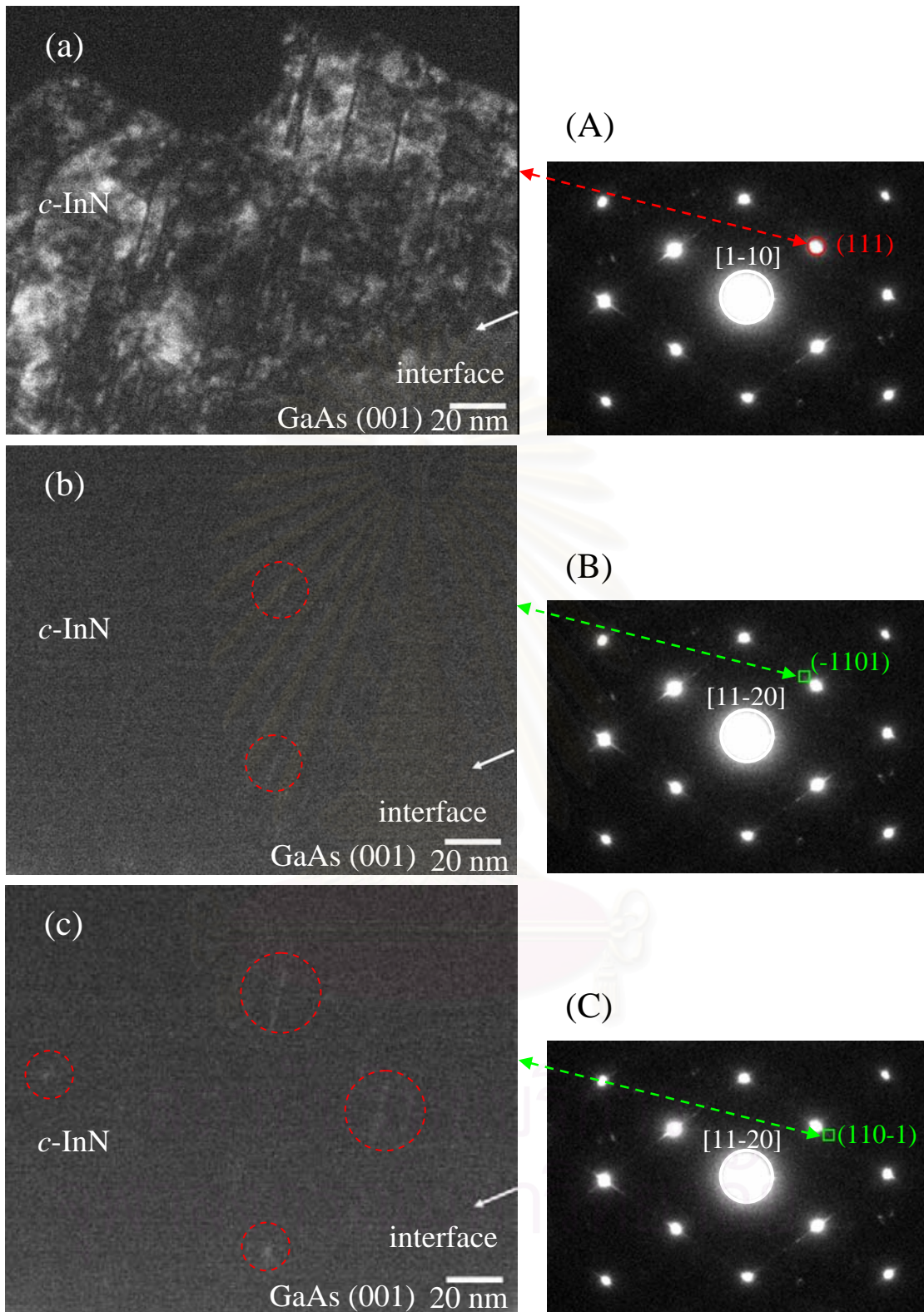


Figure 4.11: Dark field images of *c*-InN film on GaAs (001) substrate grown under the In-rich conditions (at 490°C with the N₂ flow rate of 1.5 sccm) which were taken with reflections along (a) $g = (111)$, (b) $g = (-1101)$ and (c) $g = (110-1)$ planes. Inset (A), (B) and (C) showing ED patterns were taken from (111), (-1101) and (110-1) diffraction spots shown in (a), (b) and (c), respective. Zone axes is $[1-10]//[11-20]$.

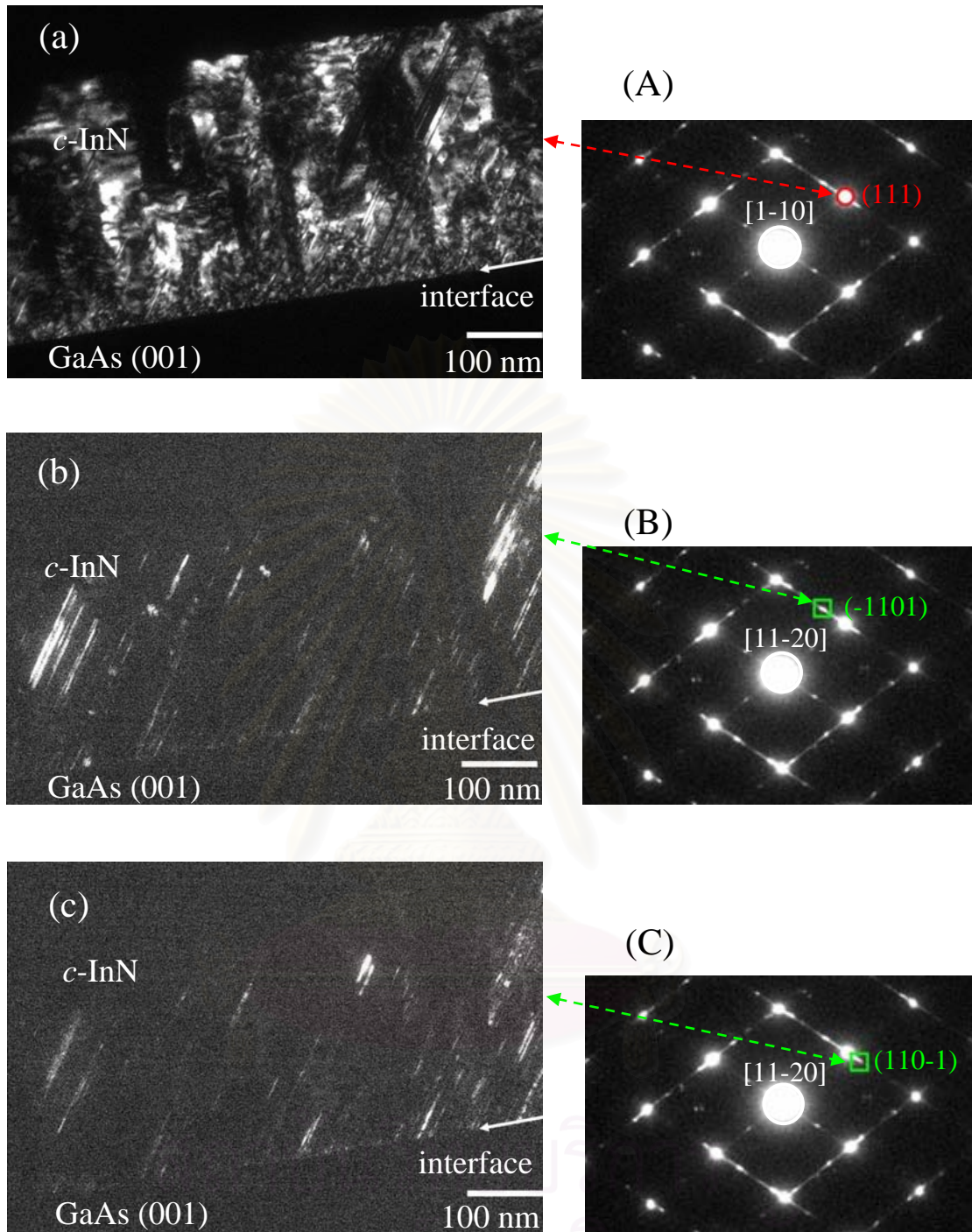


Figure 4.12: Dark field images of *c*-InN film on GaAs (001) substrate grown under the N-rich conditions (at 450°C with the N₂ flow rate of 1.75 sccm) which were taken with reflections along (a) $g = (111)$, (b) $g = (-1101)$ and (c) $g = (110-1)$ planes. Inset (A), (B) and (C) showing ED patterns were taken from (111), (-1101) and (110-1) diffraction spots shown in (a), (b) and (c), respective. Zone axes is $[1-10]//[11-20]$.

4.8 Summary

The micro-(nano-) structural investigation of the MBE grown *c*-InN samples with different growth condition (In- and N-rich growth conditions) demonstrated that the structural phase transition of InN from cubic to hexagonal structures is much dependent on the growth condition. It was found by XRD measurements and TEM observations that the InN grown layers exhibited a transition from cubic to mixed cubic/hexagonal phase under In- and N-rich growth conditions. The ED pattern in TEM measurement presents the SFs in *c*-InN film under N-rich can become seeds of the *h*-InN structure in the layer of *c*-InN. It clearly shows that {0001} plane of hexagonal phase is easily generated along {111} cubic plane. In addition, the raman scattering from these InN layers confirms the existence of transition in microstructure of the InN grown layers for N-rich growth condition. It is suggested that the growth condition is a key parameter in the growth of high cubic phase purity *c*-InN films without incorporation of single-crystal *h*-InN.

CHAPTER V

CONCLUSIONS

In the thesis, the author described a study of structural properties of the *c*-InN films grown by MBE. HRXRD and Raman scattering measurements and TEM were mainly used to investigate the structural modification, crystal structure and structural defects of the *c*-InN films. The discussion was focused on the different of growth conditions, especially the In- and the N-rich growth conditions. The main results and conclusions obtained in this research work are summarized as follows:

(1) The crystalline structure was estimate from HRXRD. The result demonstrates that all the InN grown films have cubic structure.

(2) The structural defect in the *c*-InN film grown under different growth conditions (In- and N-rich growth condition) mainly analyzed from electron diffraction (ED) patterns and cross-sectional micrograph of TEM measurements. The results demonstrate that were the InN grown film has a cubic structure. On the other hand, a high density of planar defects such as stacking faults and twins on the (111) cubic plane were clearly observed.

(3) The polytype transition of InN grown on GaAs (001) substrates by MBE was investigated. It was found by TEM observations that the InN grown layers exhibited a transition from cubic to mixed cubic/hexagonal phase under N-rich growth condition. For In-rich growth condition, no different types of single diffraction spots, indicating the incorporation of single-crystal *h*-InN, on the ED pattern was observed. In addition, the μ -Raman scattering spectra obtained from these InN layers confirm the existence of a structural modification from cubic to mixed cubic/hexagonal phase in microstructure of the N-rich layers, which exhibit higher hexagonal-phase incorporation than that of the In-rich layers. Our results demonstrate that the In-rich growth condition plays a critical role in the growth of high quality *c*-InN films with higher cubic phase purity.

It is suggested that the growth condition is a key parameter in the growth of high cubic phase purity *c*-InN films without incorporation of single-crystal *h*-InN.



สถาบันวิทยบริการ
จุฬาลงกรณ์มหาวิทยาลัย

REFERENCES

- [1] J. Ohta, K. Mitamura, A. Kobayashi, T. Honke, H. Fujioka and M. Oshima. growth of InN on nearly lattice-match (Mn, Zn) Fe₂O₄, *Solid State Communications*. **137** (2006): 208-211.
- [2] Ph. Komninou, Th. Kehagias, A. Delimitis, G. P. Dimitrakopoulos, J. Kioseoglou, E. Dimakis, A. Georgakilas and Th. Karakostas. Microstructural assessment of - on- GaN films grown by plasma-assisted MBE, *Superlattices and Microstructures*. **36** (2004): 509-515.
- [3] X. Wang and A. Yoshikawa. Molecular beam epitaxy growth of GaN, AlN and InN, *Progress in Crystal Growth and Characterization of Materials*. **48/49** (2004): 42-103.
- [4] S. V. Ivanov, T. V. Shubina, V. N. Jmerik, V. A. Vekshin, P. S. Kop'ev and B. Monerma. Plasma-assisted MBE growth and characterization of InN on sapphire, *J. Cryst. Growth*. **269** (2004): 1-9.
- [5] C.-L. Wu, C.-H. Shen, H.-Y. Chen, S.-J. Tsai, H.-W. Lin, H.-M. Lee, S. Gwo, T.-F. Chuang, H.-S. Chang and T.-M. Hsu. The effects of AlN buffer on the properties of InN epitaxial films grown on Si (111) by plasma-assisted MBE, *J. Cryst. Growth*. **288** (2006): 247-253.
- [6] J. Wu, W. Walukiewicz, K. M. Yu, J. W. Ager III, E. E. Haller, Y. Saito and Y. Nanishi. Unusual properties of the fundamental band gap of InN, *Appl. Phys. Lett.* **80** (2002): 3967-3969.
- [7] T. L. Tansley and C. P. Foley. Optical band gap of indium nitride, *J. Appl. Phys.* **59** (1986): 3241-3244.
- [8] K. Osamura, K. Nakajima and Y. Murakami. Fundamental Absorption Edge in GaN, InN and Their Alloys, *Solid State Communications*. **11** (1972): 617-621.
- [9] H. J. Hovel and J. J. Cuomo. Electrical and Optical Properties of rf-Sputtered GaN and InN, *Appl. Phys. Lett.* **20** (1972): 71-73.
- [10] A. G. Bhuiyan, A. Hashimoto and A. Yamamoto. Indium nitrides (InN): A review of growth, characterization and properties, *J. Appl. Phys.* **94** (2003): 2779-2808.

- [11] A. P. Lima, A. Tabata, J. R. Leite, S. Kaiser, D. Schikora, B. Schöttker T. Frey, D. J. As, and K. Lischka. Growth of cubic InN on InAs(0 0 1) by plasma-assisted molecular beam epitaxy, *J. Cryst. Growth*. **201-202** (1999): 396-398.
- [12] V. Cimalla, J. Pezoldt, G. Ecke, R. Kosiba, O. Ambacher, L. Spieß, and G. Teichert. Growth of cubic InN on r -plane sapphire, *Appl. Phys. Lett.* **83** (2003): 3468-3470.
- [13] M. S. Cho, N. Sawazaki, K. Sugita, A. Hashimoto, A. Yamamoto and Y. Ito. Characterization of MOVPE InN films grown on 3c-SiC/Si(111) templates, *Phys. Stat. Sol (c)* **4** (2007): 2441-2444.
- [14] T. Nakamura , T. Kataoka, R. Katayama, T. Yamamoto and K. Onabe. RF-MBE growth of cubic InN films on YSZ (001) vicinal substrates, *Phys. Stat. Sol. (c)* **5** (2008): 1712-1714.
- [15] G. Shikata, S. Hirano, T. Inoue, M. Orihara, Y. Hijikata, H. Yaguchi and S. Yoshida. RF-MBE growth of a-plane InN on r-plane sapphire with a GaN under layer, *J. Cryst. Growth* **301-302** (2007): 517-520.
- [16] H. F.Li, H. Chen, L. Wan, Z. Q.Li, Q. Huang, and J. M Zhou. Epitaxial growth and characterization of GaN film on (001) GaAs substrates by radio-frequency molecular beam epitaxy, *J. Cryst. Growth*. **227-228** (2001): 390-394.
- [17] S. Sanorpim, E. Takuma, K. Onabe, H. Ichinose, and Y. Shiraki. Laterally Overgrown GaN on Patterned GaAs (001) Substrates by MOVPE, *phys. stat. sol. (a)* **192** (2002): 446
- [18] Y. Park, M. J. Cich, R. Zhao, P. Specht, and E. R. Weber. Analysis of twin defects in GaAs (111)B molecular beam epitaxy growth, *J. Vac. Sci Technol.* **18** (2002): 1566-1571.
- [19] H. Okamura, S. Yoshida and T. Okahisa. Optical properties near the band gap on hexagonal and cubic GaN, *Appl. Phys. Lett.* **64** (1994): 2997-3000.
- [20] T. Nakamura, K. Iida, R. Katayama, T. Yamamoto and K. Onabe. RF-MBE growth and structural characterization of cubic InN films on GaAs, *phys. stat. sol. (b)* **243** (2006): 1451–1455.

- [21] Y. Iwahashi, H. Yaguchi, A. Nishimoto, M. Orihara, Y. Hijikata and S. Yoshida. RF-MBE growth of cubic InN films on MgO (001) substrates, *phys. stat. sol. (c)* **3** (2006): 1515–1518.
- [22] M. Ohring. *Materials Science of Thin Films*. 2nd ed. London: Academic Press Inc., 2002.
- [23] D. B. Holt and B. G. Yacobi. *Extended Defects in Semiconductor*. New York: Cambridge University Press, 2007.
- [24] M. Kuball. Raman spectroscopy of GaN, AlGaIn and AlN for process and growth monitoring/control, *Surface and Interface Analysis*, **31** (2001): 987-999.
- [25] Srnanek, R. et al. A Raman study of GaAsN, GaInAsN layers on beveled samples, *Mater. Sci. Eng. B*, **91-92** (2002): 87-90.
- [26] H. Yauchi, J. Baoping Zhang, Y. Segawa, H. Nagasawa K. Onabe and Y. Shiraki. Micro Raman and micro photoluminescence study of cubic GaN grown on 3C-SiC (001) substrate by metalorganic vapor phase epitaxy, *J. Cryst. Growth*. **195** (1998): 323-327.
- [27] X. L. Sun, Hui Yang, L. X. Zheng, D. P. Xu, J. B. Li and Z. G. Wang. Stability investigation of cubic GaN films grown by metalorganic chemical vapor deposition on GaAs (001), *Appl. Phys. Lett.* **74** (1999) 2827-2829.
- [28] O. Birot, B. Maleyre, S. Ruffenanch, B. Gil, C. Pinquier, F. Demangeot, J. Frandon. Absorption and Raman scattering processes in InN films and dots, *J. Cryst. Growth*. **269** (2004): 22-28.
- [29] G. Kaczmarczyk, A. Kaschner, S. Reich, A. Hoffmann, and C. Thomsen. Lattice dynamics of hexagonal and cubic InN: Raman-scattering experiments and calculations, *Appl. Phys. Lett.* **76** (2000): 2122-2124.
- [30] D. B. Williams and C. B. Carter. *Transmission Electron Microscopy, A textbook for Materials Science*. New York: A Division of Plenum Press Publishin Corporation, 1996.
- [31] B. Fultz, and J. Howe. *Transmission Electron Microscopy and Diffractometry of Materials*. 2nd ed. Tokyo: Spriger, 2002.

- [32] S. Suandon. *Structural property analysis of GaN grown on GaAs by MOVPE using transmission electron microscopy*. Master's thesis, Department of Physics, Faculty of Science, Chulalongkorn University, 2005.
- [33] J. W. Edington. *Practical Electron Microscopy in Materials Science*. Van Nostrand Reinhold Company. Delaware, 1976.
- [34] S. Kuntharin, S. Sanorpim, T. Nakamura, R. Katayama and K. Onabe. Structural Investigation of Cubic-phase on GaAs (001) Growth by MBE Under In- and N-rich Growth Conditions, *Advanced Material Research*, **31**, (2008): 215-217.
- [35] M. Balkanski and R. F. Wallis. *Semiconductor Physics and Applications*. Oxford: University Press, 2000.
- [36] M. H. Loretto. *Electron Beam Analysis of Materials*. 2nd ed. London: Chapman-Hall, 1994.



สถาบันวิทยบริการ
จุฬาลงกรณ์มหาวิทยาลัย



APPENDIX

สถาบันวิทยบริการ
จุฬาลงกรณ์มหาวิทยาลัย

Conference Presentations

1. **Papaporn Jantawongrit**, Sakuntam Sanorpim, Chanchana Thanachayanont, Teruyuki Nakamura, Ryuji Katayama, and Kentaro Onabe. Microstructure of MBE Grown Cubic InN Film on GaAs (001) Substrate. *5th Thailand Material Science and Technology Conference*, September 16-19, 2008 **(Poster presentation)**.

2. **Papaporn Jantawongrit**, Sakuntam Sanorpim, Chanchana Thanachayanont, Teruyuki Nakamura, Ryuji Katayama, and Kentaro Onabe. Microstructural studies of cubic InN on GaAs (001) grown by molecular beam epitaxy. *26th Annual Conference of the Microscopy Society of Thailand*, January 28-29, 2009 **(Oral presentation)**.

3. **Papaporn Jantawongrit**, Sakuntam Sanorpim, Chanchana Thanachayanont, Teruyuki Nakamura, Ryuji Katayama, and Kentaro Onabe. TEM Observation of Cubic-Phase InN Films Grown on GaAs (001) Substrates. *Siam Physics Congress (SPC)*, March 19-21, 2009 **(Poster presentation)**.

สถาบันวิทยบริการ
จุฬาลงกรณ์มหาวิทยาลัย

VITAE

Miss Papaporn Jantawongrit was born on March 18, 1983 in Roi-ET, Thailand. She received her bachelor degree of Science in Physics from King Mongkut's University of Technology Thonburi in 2006, and continued her Master's study at Chulalongkorn University in 2006.



สถาบันวิทยบริการ
จุฬาลงกรณ์มหาวิทยาลัย